Editor Query Form

Book title: **Aerosol Measurement: Principles, Techniques, and Applications, Third Edition**
Author: **P. Kulkarni et al.**
Chapter: **23**

The following queries have arised while correcting your proof. Please provide an answer in the right-hand column below and on your proofs. Many thanks for your help.

Query No.	Query	Response
EDQ1	Please provide all authors for Ye et al. 1999.	

PART III

APPLICATIONS

23

NONSPHERICAL PARTICLE MEASUREMENT: SHAPE FACTOR, FRACTALS, AND FIBERS

PRAMOD KULKARNI[1] AND PAUL A. BARON[1]

Centers for Disease Control and Prevention, National Institute for Occupational Safety and Health, Cincinnati, Ohio

CHRISTOPHER M. SORENSEN

Department of Physics and Program for Complex Fluid Flows, Kansas State University, Manhattan, Kansas

MARTIN HARPER[1]

Centers for Disease Control and Prevention, National Institute for Occupational Safety and Health, Morgantown, West Virginia

[1]The findings and conclusions in this chapter are those of the authors and do not necessarily represent the views of the Centers for Disease Control and Prevention.

Aerosol Measurement: Principles, Techniques, and Applications, Third Edition. Edited by P. Kulkarni, P. A. Baron, and K. Willeke

23.1 INTRODUCTION

Many aerosol measurement techniques are based on the behavior of ideal aerosol particles, that is, spherical particles with a density close to 1000 kg/m^3 [1 g/cm^3]. In dealing with most real-world particles, allowances must be made for nonspherical particle behavior. In many situations, nonideal particle behavior or property can be considered as a modification of ideal particle behavior by using a correction factor, commonly called the shape factor. Two types of particles, agglomerates (or clusters of particles) and fibers, have been dealt with extensively in the literature and are discussed in more detail in this chapter.

23.2 DYNAMIC SHAPE FACTOR OF NONSPHERICAL PARTICLES

23.2.1 Physical Descriptors

"Physical size," which most often governs the behavior of a spherical particle, can be difficult to describe for nonspherical particles with complex or irregular morphology not describable by Euclidean geometry. Instead, the concept of equivalent diameter is used to understand their transport in a given system. Often more than one equivalent diameter is necessary to capture complete dynamical behavior of nonspherical particles in a given system. A property-equivalent diameter is a diameter of a sphere with the same property as that of the nonspherical particle in question under identical conditions.

The volume equivalent diameter, d_v, is defined as the diameter of a spherical particle of the same volume as the particle under consideration. For an irregular particle, d_v is the sphere diameter that the particle would acquire if it were liquefied to form a droplet while preserving any internal void volume (i.e., internal pockets of voids isolated from the gas surrounding the particle). Some aggregates from combustion processes can have internal void volumes (Kasper 1982). For spherical particles, d_v is equal to their physical size, d_p.

The mass equivalent diameter, d_m, of a particle is the diameter of a nonporous sphere composed of the bulk particle material that has the same mass as the particle in question. Another diameter, called the envelope equivalent diameter (d_e), has also been used, which is defined as the diameter of a sphere that is composed of the bulk particle material and includes the same internal volume of voids, and has the same mass as the particle in question. In this respect, d_e is same as d_v. When a particle is nonporous and there are no internal voids, d_m, d_v, and d_e are identical. If the ratio of the volume equivalent and mass equivalent diameters is δ (i.e., $d_v = d_e = \delta\, d_m$), the void fraction of a particle is given by $(1 - 1/\delta^3)$. The factor δ accounts for the porosity of the particle.

A nonspherical particle can be described by various types of densities depending on what volume and mass is used to define them. Material density, ρ_m, is defined as the average density of the solid (and liquid) material in the particle, and is expressed in terms of the particle mass, m_p, and mass equivalent diameter as,

$$\rho_m = \frac{m_p}{\frac{\pi}{6} d_m^B} \qquad \text{(Eq. 23-1)}$$

Similarly, particle density, ρ_p, is defined with respect to volume equivalent diameter, which accounts for internal void volume, and is given by,

$$\rho_p = \frac{m_p}{\frac{\pi}{6} d_v^B} \qquad \text{(Eq. 23-2)}$$

Both the densities are related by δ as follows,

$$\rho_m = \delta^3 \rho_p \qquad \text{(Eq. 23-3)}$$

Another density called effective density (ρ_e) has also been used and is defined as,

$$\rho_e = \frac{m_p}{\frac{\pi}{6} d_B^3} \qquad \text{(Eq. 23-4)}$$

where, d_B is the electric mobility diameter of the particle, defined later.

23.2.2 Dynamic Shape Factor

The Stokes' law for drag force on a moving particle is based on the assumption of spherical shape of the particle. For nonspherical particles, the drag force depends on the shape of the particle and its orientation in the flow field. To account for departure from sphericity a drag correction factor, called dynamic shape factor (χ) is introduced. The dynamic shape factor is defined as the ratio of the drag force on a nonspherical particle (F_D) to the drag force on that particle's volume equivalent sphere (F_{Dve}) when both particles are traveling at the same relative velocity V as shown in Figure 23-1,

$$\chi = \frac{F_D}{F_{Dve}} \qquad \text{(Eq. 23-5)}$$

The above relationship leads to the following expression for the drag on a nonspherical particle in the Stokes' law regime

$$F_D = \frac{3\pi\mu d_v \chi V}{C(d_v)} \qquad \text{(Eq. 23-6)}$$

where μ is absolute viscosity of gas, V is velocity of the particle with respect to the surrounding gas, d_v is volume

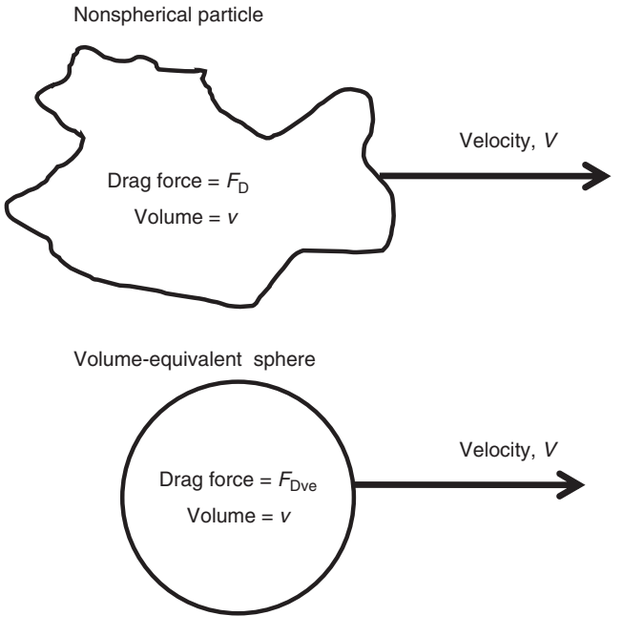

Figure 23-1 Nonspherical particle and its volume equivalent sphere. The dynamic shape factor is given by the ratio F_D/F_{Dve} when both particles are traveling at the same relative velocity, V.

equivalent diameter of the particle, and $C(d_v)$ is slip correction factor for the volume equivalent diameter. The dynamic shape factor is a function of Knudsen number, Kn (defined as the ratio of mean free path of gas to particle radius), and can assume different values in free molecule, transition, and continuum regime.

The dynamic shape factor captures deviation of particle shape from spherical shape; the shape factor of spheres is 1. A shape factor greater than 1 implies that the nonspherical particle settles slowly in air compared to its volume equivalent sphere. Dynamic shape factor for most nonspherical particles is close to or greater than 1. The shape factor can be less than 1 for some streamlined objects (Fuchs 1964). For elongated particles with high aspect ratios, the dynamic shape factor also depends on the orientation of the particle with respect to the flow field. The dynamic shape factor for random particle orientation, which typically occurs at low particle Reynolds number (<0.1), is given by,

$$\frac{1}{\chi_{ran}} = \frac{1}{3}\left(\frac{1}{\chi_{\parallel}} - \frac{1}{\chi_{\perp}}\right) \qquad \text{(Eq. 23-7)}$$

where $\chi_{\parallel}$ and $\chi_{\perp}$ are shape factors when the particle's symmetry axis is oriented parallel and perpendicular to the flow, respectively, and χ_{ran} is the orientation-averaged shape factor. Table 23-1 shows dynamic shape factors for some simple regular shapes and their configurations.

TABLE 23-1 Dynamic Shape Factors of Simple Shapes

Particle Shape	Dynamic Shape Factor, χ
Sphere	1
Cube	1.08
Cylindrical fiber, $\theta^{\alpha} = 0^{\circ}$ and 90°	
$(l/d_f = 2)$	1.01, 1.14
$(l/d_f = 5)$	1.06, 1.34
$(l/d_f = 10)$	1.50, 1.58
Compact cluster of spheres	1.15 (triplets)
	1.17 (quadruplets)

Source: Data from Hinds (1999).

θ^{α} = angle between axis of symmetry of the particle and the flow direction; l = length of fiber; d_f = diameter of cylindrical fiber.

The shape factor can also be defined in terms of mass equivalent diameter (d_m), such that,

$$F_D = \frac{3\pi\mu d_m \chi^m V}{C(d_m)} \qquad \text{(Eq. 23-8)}$$

where χ^m is shape factor based on d_m. χ^m is related to χ through following equation,

$$\chi^m = \chi\frac{\delta C(d_m)}{C(\delta d_m)} \qquad \text{(Eq. 23-9)}$$

where δ is the porosity factor introduced earlier. The above formulation in terms of χ^m is particularly important in case of an aggregate or agglomerate with internal voids. For such particles, $d_m < d_v$, which implies, $\rho_m > \rho_p$ and $\chi^m < \chi$. In the above equation, χ accounts for the effect of external shape on drag, while δ accounts for the porosity component. Therefore, deviation of χ^m from a value of 1 does not necessarily mean departure from the spherical shape, as in the case of χ^m. For nonporous particles (with no internal voids; $\delta = 0$), χ and χ^m are identical. Figure 23-2 shows the relationships between the two definitions of dynamic shape factors with various particle morphologies. Caution should be exercised in distinguishing parameters between the two formulations of shape factors and the associated two parallel set of parameters describing volume, density, and property equivalent diameters.

Morphological features of agglomerate particles from the data of Kops et al. (1975), Van de Vate et al. (1980), Allen and Briant (1978), Allen et al. (1978, 1979), Kasper and Shaw (1983), and Stöber et al. (1970) can be categorized into two groups: (1) a branched-chain structure (agglomerate in Fig. 23-2a) and (2) a compact aggregate with a more discernible envelop shape (agglomerate in Fig. 23-2c). The dynamic shape factors of each of these two morphologies are also distinct. For the branched-chain aggregates, the dynamic shape factor increases with the addition of primary spheres to the aggregate and is directly proportional to the

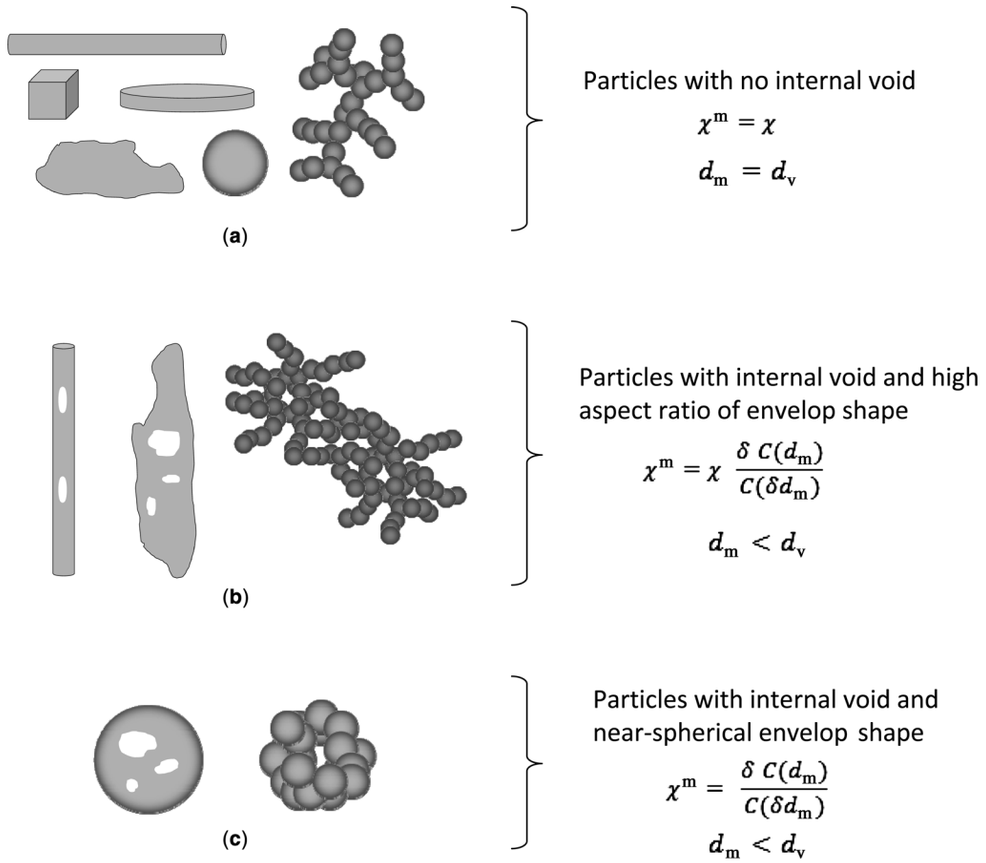

Figure 23-2 Relationship between χ and χ^m for different particle morphologies.

cube root of the total number of primary particles (Stöber 1972; Kops et al. 1975; Allen and Bryant 1978; Allen et al. 1978). This behavior is consistent with particles' shapes determining their dynamic shape factors χ^m (Fig. 23-2a).

In compact agglomerates with internal voids, the porosity factor δ dominates the dynamic shape factor χ^m. For compact agglomerates, the shape factor is relatively independent of the number of primary particles but depends rather on the packing density of the primary particles in the aggregate (Kops et al. 1975; van de Vate et al. 1980). This behavior is consistent with the porosity of the agglomerate determining its dynamic shape factor χ^m (Fig. 23-2c).

23.2.3 Slip Correction Factor

Determination of the slip correction factor of nonspherical particles from experimental data has always been challenging due to the inseparable nature of slip correction and the dynamic shape factor (Allen and Raabe 1985). Equation 23-2 uses equivalent volume sphere to calculate slip correction. This approach, termed as equivalent sphere approach (ESA) by Dahneke (1973a,b,c), is adequate for most nonspherical particles with relatively small aspect ratios. However, this approach also leads to a slight particle size dependence of shape factor in the transition regime. For thin and long slender bodies, such as needles and thin disk-like particles, the ESA approach ignores the effect of particle orientation on the slip correction. To account for these effects Dahneke (1973a,b,c) proposed an adjusted sphere approach (ASA) applicable over the entire range of Knudsen number. The ASA approach involves calculating the size of an "adjusted sphere," which has the same slip correction factor as that of the nonspherical particle under consideration in the free molecule regime, such that the drag is given by,

$$F_D = \frac{3\pi\mu d_v \chi_c V}{C(d_{adj})} \qquad \text{(Eq. 23-10)}$$

where χ_c is dynamic shape factor in the continuum regime, and d_{adj} is the adjusted sphere diameter. This adjusted diameter provides an accurate value of slip correction when both $Kn > 10$ and when $Kn \to 0$, since the slip correction is always unity in the latter case. The transition regime shape factor (χ) is given by $\chi = \chi_c(C(d_v)/C(d_{adj}))$. The approach allows calculation of slip correction over the transition regime that asymptotically approaches the two limits in the

two extremities of free molecule and continuum regimes (Dahneke 1973a,b,c; Cheng et al. 1988a,b). The ASA approach can be used for particles that can be described by regular shapes such as cylinders, prolate or oblate spheroids, disks, and so on, for which the drag in the continuum as well free molecule regimes can be calculated. Chen et al. (1993) also noted that using the correct shape and morphology is quite important in determining the adjusted sphere diameter. Table 23-2 shows slip correction factors for fiber particles using both the approaches. The differences in slip correction can be significant when describing the influence of orientation at high aspect ratios.

Using volume equivalent sphere for calculation of slip correction in Equation 23-2 leads to Kn dependence of χ. Numerical and experimental evidence on simple shapes such as cylinders, chains of spheres, spheroids, and cubes, suggests that the dynamic shape factors in both free molecule and continuum regime are approximately equal up to a value of about 2; above that, continuum regime shape factors are larger than those in the free molecule regime (DeCarlo et al. 2004; Zelenyuk et al. 2006).

23.2.4 Measurement of Dynamic Shape Factor

23.2.4.1 Property-Equivalent Diameters of Nonspherical Particles In addition to the property-equivalent diameters defined above, several other equivalent particle diameters are defined. Measurement of multiple property-equivalent diameters is often necessary to obtain dynamic shape factor.

The electric mobility diameter, d_B, of a particle is the diameter of a sphere with the same electrical mobility and charge as the particle under consideration. Diffusion equivalent diameter, that is, the diameter of a sphere with the same thermal diffusivity as the particle under consideration, can be determined from its electric mobility when the electrical charge on the particle is known. The aerodynamic equivalent diameter, or aerodynamic diameter, d_a, of a particle is the diameter of a sphere of unit specific gravity that settles at the same terminal velocity as the particle. Strictly speaking, these diameters are a function of Knudsen number due to their dependence on slip correction factor. Measurements in electrical mobility analyzers (see Chapter 15) are typically conducted in transition regime ($0.1 < Kn < 10$). Depending on the size range of particles and the techniques employed, aerodynamic diameters can be measured in continuum (sedimentation or Millikan cells), transition (inertial impactors), or free molecule regime (single particle mass spectrometers). These equivalent diameters are related by the dynamic shape factor χ, the particle density ρ_p, and the standard density $\rho_0 = 1000\ \mathrm{kg/m^3}$ [$1\ \mathrm{g/cm^3}$], and by the effective density ρ_e.

TABLE 23-2 Comparison of Slip Correction Factor Calculated from ESA[a] and ASA[b] Approaches for Fibers[c] with Length to Diameter Ratio of 20

Kn	Orientation, θ^d	$C(d_v)$	$C(d_{adj})$
0.5	0°	1.23	1.33
0.5	90°	1.23	1.2
0.5	Random	1.23	1.26
1	0°	1.47	1.69
1	90°	1.47	1.41
1	Random	1.47	1.53
2	0°	2.00	2.49
2	90°	2.00	1.87
2	Random	2.00	2.13

Source: Data from Dahneke (1973c).

[a]Using equivalent volume diameter, d_v.

[b]Using adjusted sphere diameter, d_{adj}.

[c]Calculation based on a prolate spheroid, assumed to represent cylindrical particles, with a major-to-minor axis ratio of 20.

[d]Angle between symmetry axis and flow direction.

The aerodynamic diameter is related to its volume equivalent diameter (d_v) through the following relationship (Hinds 1999),

$$d_a = d_v \sqrt{\frac{\bar{\rho}_p}{\chi} \frac{C(d_v)}{C(d_a)}} \qquad \text{(Eq. 23-11)}$$

where $\bar{\rho}$ is particle density (ρ_p) normalized by the standard density (ρ_0); $C(d_v)$ and $C(d_a)$ and are slip correction factors for diameters d_v and d_a, respectively; χ is the dynamic shape factor of the particle in the transition regime.

The relationship between electrical mobility diameter d_B and d_v can be obtained by equating the drag in terms of mobility diameter ($= 3\pi\mu d_B V/C(d_B)$) to that in terms of χ and d_v ($= 3\pi\mu d_v \chi V/C(d_v)$), which leads to the following expression for dynamic shape factor in the transition regime,

$$\chi = \frac{d_B}{d_v} \frac{C(d_v)}{C(d_B)} \qquad \text{(Eq. 23-12)}$$

Using Equations 23-11 and 23-12, d_v can obtained as,

$$d_v = \left(\frac{d_a^2 d_B}{\bar{\rho}_p} \frac{C(d_a)}{C_c(d_B)} \right)^{\frac{1}{3}} \qquad \text{(Eq. 23-13)}$$

Thus volume equivalent diameter can be obtained from the above equation, once the values of aerodynamic and mobility diameter, and particle density are known. Once d_v is known, the dynamic shape factor can be obtained using Equation 23-12. Particle mass, m_p, is given by

$$m_p = \frac{\pi}{6} d_a^2 d_B \frac{C(d_a)}{C(d_B)} \rho_0 \qquad \text{(Eq. 23-14)}$$

and the effective density, ρ_e, is given by,

$$\rho_e = \frac{d_a^2}{d_B^2} \frac{C(d_a)}{C(d_B)} \rho_0 \qquad \text{(Eq. 23-15)}$$

Equations 23-11 to 23-15 can be used to derive various parameters once the aerodynamic and mobility diameters, and particle density (ρ_p) are known. Both m_p and ρ_e can be derived from measured d_a and d_B directly, whereas particle density (ρ_p) must be additionally known to estimate values of χ and d_v.

23.2.4.2 Experimental Techniques Early measurements of dynamic shape factors were performed with Millikan cells (Fuchs 1964; Chen et al. 1993), a combination of aerosol centrifuge and microscopy (Stöber 1972; Kasper 1977), or sedimentation cell, and mass and number concentration measurements (Wu and Colbeck 1996). Since these techniques are time- and resource-intensive, they have been largely replaced by real-time measurement techniques which provide *in situ*, near-real-time measurement of particle properties, particularly in the submicrometer size range. Tandem measurements involving size selection (or classification) using a differential mobility analyzer (DMA; Chapter 15), followed by additional property measurement of the size-selected (or classified) aerosol have been commonly used (Park et al. 2008). The tandem techniques exploit the relationships between various property-equivalent diameters discussed above. As noted earlier, out of five parameters d_B, d_a, d_v, χ, and m_p, independent measurement of any three parameters can be used to determine the other remaining parameters through iterative solution of Equations 23-11 to 23-15. Mobility and aerodynamic diameters and particle mass m_p can be measured directly using a variety of instruments. After mobility classification in DMA (to obtain an aerosol with known d_B), d_a can be measured in tandem using either impactors (Kelly and McMurry 1992; Hering and Stolzenberg 1995; de la Mora et al. 2003), aerodynamic particle sizers (Kasper and Wen 1984; Brockmann and Rader 1990), single particle mass spectrometers (Slowik et al. 2004; Zelenyuk et al. 2006; Schneider 2006), or electrical low pressure impactors (Maricq et al. 2000; Van Gulijk et al. 2004). Particle mass (m_p) can also be determined using aerosol particle mass analyzers in tandem (McMurry et al. 2002; Park et al. 2003) or tapered element oscillating microbalances operating in parallel (Morawska et al. 1999; Pitz et al. 2003). Volume equivalent diameters can be measured using microscopy (Kasper 1977; Park et al. 2004) or a combination of mass and number concentration measurements (Wu and Colbeck 1996).

Studies involving tandem measurements techniques have mainly dealt with measurement of particle's effective density, ρ_e (Kelly and McMurry 1992; Karg 2000; McMurry et al. 2002; Park et al. 2003; Khlystov et al. 2004; Slowik et al. 2004). Effective density describes the combined effect of particle density and its shape on its transport and can be readily obtained using only two diameters, d_B and d_a. An additional measurement of particle mass (m_p) or particle density (ρ_p) will be necessary to derive dynamic shape factor. In many cases, particle density is known *a priori* or can be approximated, allowing measurement of dynamic shape factor using only two measured parameters d_B and d_a.

Shape factors obtained from tandem measurements can suffer from many errors depending on the instruments used. The preferential orientation of nonspherical particles, particularly those with high aspect ratio, in the high electric field in the DMA must be considered when interpreting the data. Large fibers (>0.1 μm) can align themselves parallel to the electric field at field strengths less than 1 kV/cm (Lilienfeld 1985), which are often exceeded in DMAs. Similar alignment effects have been observed in DMA for chain agglomerates of spherical particles (Kousaka et al. 1996; Zelenyuk and Imre 2007) and nanowires (Kim et al. 2007; Kim and Zachariah 2005). The orientation effects must be carefully considered in interpreting the value of χ. Also, most instruments used in tandem measurements measure distribution of property; they have a varying degree of accuracy, precision, and dynamic range. These factors must be carefully considered when calculating measurement uncertainties. Multiple charging of large nonspherical particles in DMA can be a cause for concern, as this can lead to multiple subpopulations of particles in the classified aerosol with different diffusion equivalent diameters, resulting in a significant bias in the downstream measurements. The difference in flow regimes in different instruments must also be considered since d_a, d_B, and χ depend on the Knudsen number.

23.3 FRACTAL PARTICLES

23.3.1 Introduction

Nonspherical particles that can be described using fractal geometry are called fractal particles. Fractals are scale invariant objects. This means that they have dilation symmetry, that is, they look the same on all scales. Mathematical examples include the Koch curve, which has bumps upon bumps upon bumps, or the Sierpinski gasket, which has a descending series of holes, or the "dog chow" symbol shown in Figure 23-3, which has some similarity to the aggregates to be described here. Mathematical fractals are scale invariant over all scales, yet nature provides many examples of objects that are fractals over a finite range of scales. Examples include coastlines, which display inlets and peninsulas on a large scale (e.g., the western coastline of the island of Great Britain), and similar bumps and wiggles at much finer scale (e.g., a local map of a few miles of coastline). This scale invariance is not present in simple geometric objects. Thus, changing the scale of a circle makes it flatter or rounder; similarly, a square's corners get farther or closer apart. Fractal and geometric objects differ in another very important manner and that is in their dimensionality, a quantifiable parameter. Geometric objects have integer dimensions, while fractals

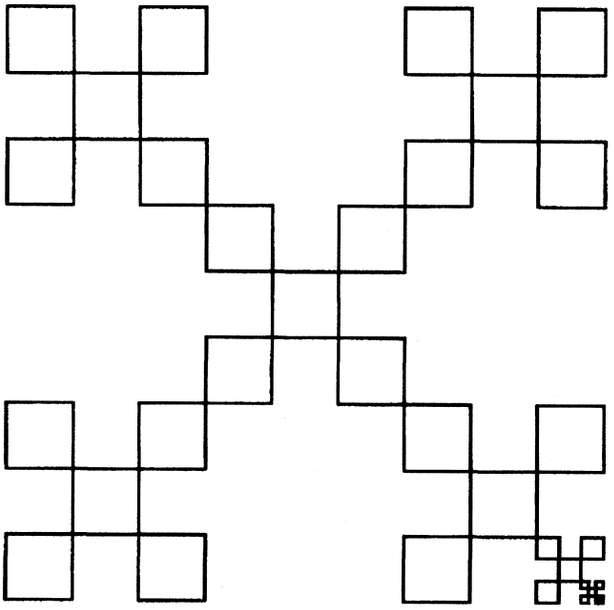

Figure 23-3 "Dog Chow" fractal with $D_f = \ln 5/\ln 3 = 1.465$. The pattern of five boxes in a larger box with three times the side length continues to all scales as implied by the box in the lower right.

have noninteger, fractal dimensions, D_f. An excellent introductory description of fractals is given by Family (1991).

The mathematical background of fractals and their relevance to natural objects put forward by Mandelbrot (1977, 1983) allowed Forrest and Witten (1979) to experimentally establish that random aggregates of metal smoke particles over a finite range of scales were fractals with a noninteger dimension. This seminal work caused an explosion of subsequent interest involving both simulation of aggregation mechanisms and experimental work on aggregation in colloids and aerosols that continues today. The purpose of this section is to describe methods whereby the size and morphological parameters of fractal aggregates (i.e., aggregates composed of simple particles that display fractal morphology) can be determined.

23.3.2 Fractal Aggregates

A fractal aggregate is an aggregate or cluster of particles that displays fractal scaling over the length scales from the primary or monomer particle size to the overall size of the aggregate. Fractal aggregates occur in aerosols and colloids as a result of random aggregation. Examples of both soot and titania fractal aggregates are given in Figures 23-4 and 23-5. The motion can be either diffusive, ballistic (straight line), or in the crossover between these, and the resulting aggregate will be a fractal within the scale limits monomer to overall aggregate size. Both computer simulation and experiments have been important in establishing our knowledge of fractal

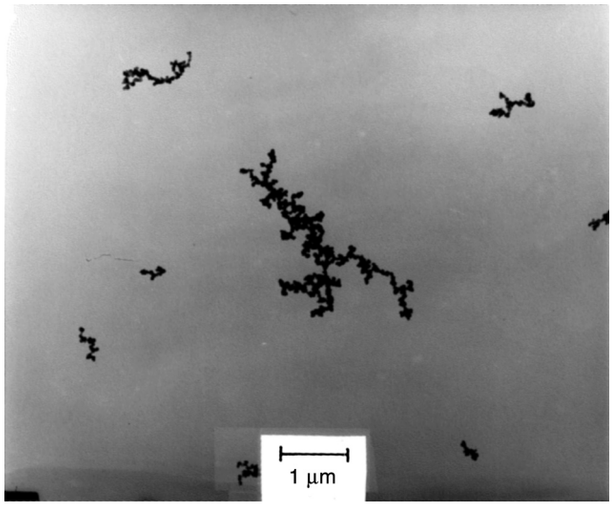

Figure 23-4 Soot fractal aggregates from a premixed methane flame. The fractal dimension is $D_f \approx 1.8$.

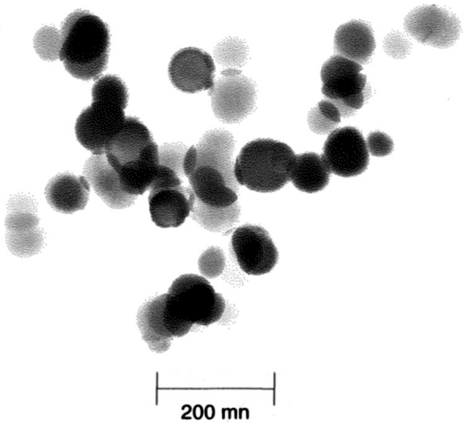

Figure 23-5 Transmission electron microscope picture of titania (TiO_2) fractal aggregates with $D_f \approx 1.8$ produced by pyrolysis of titanium isopropoxide.

aggregates (Family and Landau 1984; Meakin 1988; Viscek 1992) because aggregation can be readily simulated on the computer. An example of a computer-generated fractal aggregate is given in Figure 23-6, and the similarity to the real-world examples given in Figures 23-4 and 23-5 is apparent. We now know that the aggregates can be classified into two major categories:

1. Particle–cluster aggregation or diffusion limited aggregation (DLA), which occurs when single monomers diffuse to and stick to a stationary, growing cluster (Witten and Sander 1981). In three dimensions the clusters that result have a fractal dimension of $D_f = 2.5$. It has been shown that those aggregates are not fractal

over the entire range of their length scales (Oh and Sorensen 1998).

2. Cluster–cluster aggregation or diffusion limited cluster aggregation (DLCA or DLCCA), which occurs when all clusters diffuse and then stick when they randomly touch (Kolb et al. 1983; Meakin 1983). In three dimensions the clusters that result have a fractal dimension of $D_f \approx 1.75$ when the cluster motion is diffusive. Ballistic motion causes $D_f \approx 1.9$ (Meakin 1984). If the sticking probability is significantly less than one, the reaction limited cluster aggregation (RLCA) regime is entered, for which $D_f \approx 2.15$, a situation important for many colloids (Lin et al. 1990). It is now known that only cluster-cluster aggregates occur in aerosols and colloids, with the DLA morphology finding application in other areas.

The meaning of the fractal dimension is in the relation between linear and volumetric size, the latter of which is linearly related to the mass or number of primary particles per aggregate N. If R is a linear size of the aggregate, then $N \propto R^{D_f}$. We say that "the mass" N scales with linear size to the fractal dimension D_f. The linear size should be a geometric size, that is, a size related only to its geometry and nothing else. Thus R can be a radius or a diameter, a length or width, or a radius of gyration. Strictly speaking, it cannot be a mobility radius ($= d_B/2$), which depends not only on the linear geometric size but the flow situation as well. Geometric objects scale with their linear size as well, for example, the volume of a sphere increases by a factor of eight when the diameter is doubled because its dimensionality is three. Other dense objects display this scaling; for example, the human being if made twice as tall and kept in proportion would weigh eight times as much (and have four times the surface area). In contrast to this "ordinary" geometry, fractals have a noninteger dimension D_f, less than the embedding spatial dimension d, that is, $D_f < d$.

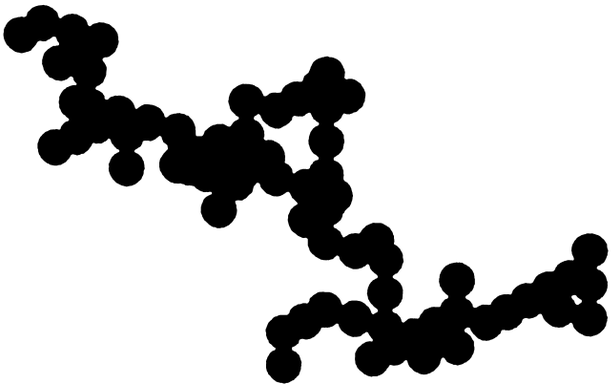

Figure 23-6 A simulated DLCA aggregate with $D_f = 1.79$.

One beauty of the fractal dimension is that it allows a quantitative description of the degree of openness, or ramification, of the random aggregate. The smaller the D_f relative to the spatial dimension d, the more quickly the aggregate fills space as R increases. The fractal dimension plays a part in determining the aggregate density, the optical properties, the way in which it diffuses, and the kinetics of its further growth.

The relation between "mass" and linear size for a fractal aggregate can be quantified in three ways, all of which will form a basis for measurement of D_f to be described below (Section 23.3.3). We let a be the monomer (primary particle) radius and R_g be the radius of gyration (a root mean square radius, Equation 23-19 below) of the aggregate. Then

$$N = k_o(R_g/a)^{D_f} \qquad \text{(Eq. 23-16)}$$

In Equation 23-16 k_o is a constant of order unity (Wu and Friedlander 1993), perhaps best described by $k_o \approx 1.3$ to 1.4 (Cai et al. 1995a; Oh and Sorensen 1997; Sorensen and Roberts 1997) but see also Köylü et al. (1992). This is perhaps the most important defining relation for a practical description of a fractal aggregate. Another important relation describes the spatial correlation function of the density $g(r)$ given by

$$g(r) \approx r^{D_f - d} h(r/\xi) \qquad \text{(Eq. 23-17)}$$

where $g(r)$ is a conditional probability relating on average the density at two points separated by a distance r. The function $h(x)$ is a cutoff function for the power law, $h(x < 1) \approx 1$, but $h(x)$ decreases more rapidly than any power law for $x > 1$. This implies that the length ξ is on the order of the size of the aggregate. For DLCA the Gaussian $h(x) \approx \exp(-x^2)$ is fairly accurate (Sorensen et al. 1992a; Cai et al. 1995a; Sorensen and Wang 1999). A third valuable relation involves the amount of material within regions of side length s centered on the aggregates. For a fractal particle

$$N \approx s^{D_f} \qquad \text{(Eq. 23-18)}$$

All three of these equations will be used for the particle analysis described below.

23.3.3 Real-Space Analysis

23.3.3.1 Collection Methods

23.3.3.1.1 Thermophoretic Collection Often aerosols are hot, for example, soot in a flame or metal oxides from a reactor, and insertion of a colder probe will cause thermophoresis of the hot aerosol particles down the thermal gradient to the colder probe. The great advantage of thermophoresis is that all particle sizes move at the same rate, hence the sampling

is unbiased (Rosner et al. 1991) at least for submicrometer particles, see Sorensen and Feke (1996).

A "frog tongue" probe device designed after Dobbins and Megaridis (1987) has been used to sample flame soot and TiO_2 and SiO_2 aerosols with apparent success (Cai et al. 1993). This device was built from a modified disk hard drive and a carbon arrow shaft. The essential quality is the ability to quickly inject a probe into the aerosol, hold it there for a residence time determined by the operator, and then quickly remove the probe. The device can move the probe 5 cm in 3 msec and has a selectable residence time of 15 to 150 msec.

The "frog tongue" part of the probe is a thin "knife blade" of metal. Transmission electron microscope (TEM) copper grids are mounted on the blade with polystyrene cement. This cement is easily broken so that the grid can be removed. The grids consist of copper mesh, having either a carbon or Formvar® coating. The blade is inserted with its face parallel to the aerosol flow to avoid perturbation of the flow and impaction of particles.

23.3.3.1.2 Impaction Collection Placing a probe with its face perpendicular to the aerosol flow will allow impaction of aggregates onto the probe. This approach was used to collect soot particles 1 μm-sized or larger (Sorensen and Feke 1996; Sorensen et al. 1998). Impaction relies on inertia so there is a bias toward collecting a larger fraction of the bigger aggregates. The Stokes number quantifies the likelihood of impaction and is discussed in Chapters 2 and 8.

23.3.3.1.3 Collection by Settling Often the aerosol settles out to form a powder at the bottom or on the sides of the chamber, container, room, or region of aerosol study. This powder can be carefully collected and redispersed to create samples for microscopic examination. Collection should proceed with some care because the fractals may be fragile, as implied by their tenuous nature. Little is known about the fragility of fractal aggregates. Experiments exist in which aggregates have been stretched and then snapped back (Friedlander et al. 1998). These imply considerable resiliency. Despite this, any reasonable caution when handling would not be wasted.

Redispersion has been accomplished using volatile liquids, perhaps with surfactants, and then drying. Water, ethanol, and acetone have been used to study carbonaceous soot and TiO_2. Water has a large surface tension and this tends to crush the aggregate as it dries. Aerosol methods have been used for redispersion of soot (Prenni et al. 2000), though it has not been established that individual particles retain their original structure. Each type of material has its own peculiarities, so experimentation is warranted.

In all cases collection densities on the microscope substrate, for example, TEM grid, should not be great, the aggregates occupying 10% of the area or less (Cai et al. 1993). This is necessary to avoid significant "artificial" aggregations on the substrate. If two aggregates overlap on the substrate, there is no way to distinguish the resulting cluster from one that formed in the aerosol phase.

23.3.4 Analysis of Projected Images

23.3.4.1 Visualization An electron microscope is necessary to study nearly all conceivable fractal aggregates since the primary particles (or monomers) are smaller than optical wavelengths ("big" particles do not stick together readily). Standard carbon- or Formvar-coated copper grids are sufficient to hold the sample. The magnification should be large enough to allow an accurate measurement of the monomer. For example, soot is usually composed of aggregates of monomers with radii $a \approx 10$ nm. To magnify these to 1 mm images requires 100,000× magnification.

Photographs can be digitized with a digital scanner for computer analysis. The image data will be in the form of a two-dimensional array with a magnitude representing the gray level at a given pixel. A computer analysis routine can be written to identify individual clusters in the digitized array, or the operator can look at the image on the monitor, pick out the images visually and store them as separate gray level arrays, one for each cluster. Often it is useful to subtract a background from this cluster gray level. The background is the average gray level of the pixels near the circumference of cluster. With this subtraction, all the nonaggregate pixels are set to zero ("white"). Once a gray level array for each cluster is achieved, analysis for morphological parameters can begin.

A major problem in the analysis of the cluster morphology is that the three-dimensional structures are viewed as two-dimensional projections as a consequence of the microphotography. One way to overcome this is to view the clusters in at least two different projections, and with this stereo technique, regenerate the true three-dimensional structure. This has been done in the past (Sampson et al. 1987; Köylü et al. 1995) but the method is laborious and, as will be shown, largely unnecessary. If the analysis is limited to one projection, and if the density of this projection can give accurate information regarding the total mass along a given projection through the cluster, then a viable analysis of the three-dimensional morphology can be obtained. Such a mass-preserving image is difficult to achieve, however, because the attenuation of the electrons producing the projected image is not linearly related to the total mass of material through which the electrons passed. Furthermore, the response of the photographic film that captures the image is linear only over a small range before it saturates and becomes insensitive to the mass of the cluster above it. In previous work involving small soot clusters (Cai et al. 1993), some success was achieved with mass-preserving projections, largely because the clusters were small enough

to keep the gray level to projected-mass relationship approximately linear. In general, however, mass-preserving projection is uncertain, so we are left with projection of the cluster onto the two-dimensional plane in a binary format, that is, a shadow, in which any part of the cluster is the same degree of gray (black) as any other, and the background is white. The advantage of this method is that it eliminates the response of the detector. The conversion to a binary format appears not only easier to apply, but is also the most reliable and accurate. What is needed is a quantitative method to convert two-dimensional information into three-dimensional information, and such a method is presented below. The bulk of the discussion applies to DLCA aggregates with $D_f \approx 1.75$, which are very typical. When $D_f > 2$, the problem of determining the size parameters of aggregates is much less explored, but a possible direction will be suggested.

23.3.5 Binary Projection Analysis

23.3.5.1 The Radius of Gyration We first consider the radius of gyration R_g of a three-dimensional body as given by

$$R_g^2 = \frac{\int r^2 \rho(r)\, d^3 r}{\int \rho(r)\, d^3 r} \qquad \text{(Eq. 23-19)}$$

where $\rho(r)$ is the density. A reasonable assumption is made that an ensemble of clusters on a TEM grid when viewed from one direction will yield an average spherical symmetry. Then, since $r^2 = x^2 + y^2 + z^2$, and since a projection onto a plane eliminates one of the dimensions, it follows from Equation 23-19 that (Cai et al. 1993)

$$R_{g,3} = \sqrt{3/2}\, R_{g,\text{proj}} \qquad \text{(Eq. 23-20)}$$

In Equation 23-20, $R_{g,3}$ is the true, three-dimensional radius of gyration of the cluster and $R_{g,\text{proj}}$ is that observed for the mass-preserving projected image. The factor $3/2$ results from the elimination of one of the three dimensions. Furthermore, it is important to stress, Equation 23-20 applies to a mass-preserving projection. Equation 23-20 is verified by the computer simulations of Köylü et al. (1995), who found the empirical factor relating the two radii to be 1.24 ± 0.01, in good agreement with $\sqrt{3/2} = 1.225$.

The previous discussion shows the difficulty in achieving an accurate mass-preserving projection, so Equation 23-20, while informative, is of questionable utility. The purpose here is to show that a better measurement can be obtained, ironically, with a two-dimensional binary representation of the cluster. Such a projection is not mass preserving because if two sections of the aggregate overlap during the projection, they cause the same darkening of the two-dimensional image as either would alone due to the binary format. It is well established that the fractal dimension of $d = 3$ DLCA clusters is less than 2; typically, D_f is in the range 1.7–1.8. Thus, it might be expected that the image of a cluster projected onto a plane in a binary format would be mass preserving, that is, no significant screening or occultation between monomers would occur. This would imply that the number of monomers in the aggregate would be proportional to the projected area of the cluster, that is, $N \propto A_c$. It must be stressed that this expectation is only correct for asymptotically large ($N \to \infty$) clusters. For finite size clusters, however, screening occurs and it is found empirically that

$$N = A_c^{\alpha} \qquad \text{(Eq. 23-21)}$$

where $\alpha = 1.1$ (for references and a complete discussion see Section 23.3.5.2). Thus, the effective fractal dimension in the two-dimensional plane of the binary projection should be different from the fractal dimension of the real, three-dimensional cluster. In the immediately following argument, we will call these fractal dimensions $D_{f,2}$ and $D_{f,3}$, respectively.

Consider how the three-dimensional cluster is projected onto the two-dimensional plane. With spherical or circular symmetry, we assume the density profile of either the three-dimensional fractal cluster or its projection is given by

$$\rho(r) \propto r^{D_f - d}, \quad \text{for } r \le R_p \qquad \text{(Eq. 23-22a)}$$

$$= 0, \quad \text{for } r > R_p \qquad \text{(Eq. 23-22b)}$$

where R_p is the perimeter radius and $D_f = D_{f,2}$ or $D_{f,3}$, depending on the spatial dimension of $d = 2$ or 3 for the binary projected or real cluster, respectively. Then Equation 23-19 yields

$$R_{g,3}^2 = \frac{D_{f,3}}{D_{f,3} + 2} R_p^2 \qquad \text{(Eq. 23-23)}$$

$$R_{g,\text{binary}}^2 = \frac{D_{f,2}}{D_{f,2} + 2} R_p^2 \qquad \text{(Eq. 23-24)}$$

Thus, a relation between the true radius of gyration $R_{g,3}$ and the measured, binary projection radius of gyration $R_{g,\text{binary}}$ can be determined if we have a relation between $D_{f,3}$ and $D_{f,2}$.

To determine this latter relation, consider the empirical fact of Equation 23-21 that $N_3 \approx A_c^{\alpha}$, where we now label the number of monomers per cluster with a subscript of three to designate that this is the number in three-dimensional space (i.e., the true number). We also have by Equation 23-16 the relation $N_3 \approx R_{g,3}^{D_{f,3}}$. The binary projection has analogous relations such that $N_2 \approx R_{g,\text{binary}}^{D_{f,2}}$ which defines $D_{f,2}$, but, and here is the key, $N_2 \approx A_c$. Furthermore, by Equations 23-23 and 23-24, $R_{g,3} \approx R_{g,\text{binary}}$. All these proportionalities

together yield

$$D_{f,2} = D_{f,3}/\alpha \qquad \text{(Eq. 23-25)}$$

This result is consistent with past work that has measured the fractal dimension of clusters both in terms of three-dimensional quantities and projectional quantities, where it was found that the projectional dimension is typically 10% less than that determined with the three-dimensional quantities (Sampson et al. 1987; Zhang et al. 1988; Cai et al. 1993). It is also consistent with simulations by Jullien et al. (1994), who also found the projectional fractal dimension to be about 10% less than the fractal dimension of the unprojected clusters. Since $\alpha \approx 1.1$, we believe Equation 23-25 explains these past observations. Finally, we use Equations 23-23 to 23-25 to find

$$R_{g,3} = \left(\frac{D_{f,3} + 2\alpha}{D_{f,3} + 2}\right)^{1/2} R_{g,\text{binary}} \qquad \text{(Eq. 23-26)}$$

Now recall that $R_g \equiv R_{g,3}$ and $D_f \equiv D_{f,3}$. Then for typical values of $D_f = 1.8$ and $\alpha \approx 1.1$, this correction factor is 1.026. Thus, as anticipated and qualitatively explained earlier (Cai et al. 1993), the binary projection yields a remarkably accurate measure of the true, three-dimensional radius of gyration.

Computer analysis of the clusters begins with the total gray level defined as

$$G_{tot} = \sum_{x,y} G(x, y) \qquad \text{(Eq. 23-27)}$$

where $G(x, y) = 0$ or 1 is the gray level of the pixel at position (x, y). Since $G(x, y)$ is binary, G_{tot} is the total number of pixels in a cluster. To determine the radius of gyration R_g of a cluster, first calculate the cluster center of mass:

$$\vec{r}_{cm} = G_{tot}^{-1} \sum_{x,y} G(x, y)\vec{r}(x, y) \qquad \text{(Eq. 23-28)}$$

and then the radius of gyration

$$R_{g,\text{binary}}^2 = G_{tot}^{-1} \sum_{x,y} G(x, y)(\vec{r}(x, y) - \vec{r}_{cm})^2 \qquad \text{(Eq. 23-29)}$$

Correction using Equation 23-26 to obtain $R_g/R_{g,3}$ could now be made, but since the correction is only about 2%, this is hardly warranted given that other experimental errors are most likely larger. Another useful and fairly simple method to determine R_g is using the maximum, projected length of the aggregate image. Computer simulations indicate that half this length (hence a radius) R_2 is a constant ratio to R_g independent of N. This is shown in Figure 23-7. The result is that

$$R_g/R_2 = 0.69 \pm 0.03 \qquad \text{(Eq. 23-30)}$$

Similar values have been found by Köylü et al. (1995) who found 0.67 (no error quoted) for $N > 100$ and Brasil et al. (1999) who found 0.667 ± 0.02 for $500 > N > 10$.

This method is simpler than calculation of R_g from the gray level, Equation 23-29, but relies on the clusters being DLCA with $D_f \approx 1.79$, that is, equivalent to the simulation that produced Figure 23-7.

23.3.5.2 Determination of N Determination of the number of monomers per aggregate N from the projected area of a cluster has a long and well established history for DLCA ($D_f \approx 1.75$) (Medalia 1967; Medalia and Heckman 1969; Mandelbrot 1977; Sampson, Mulholland, and Gentry 1987; Megaridis and Dobbins 1990; Köylü, and Faeth 1992; Cai et al. 1993; Köylü et al. 1995) Brasil et al. 1999). In general it is found that

$$N = k_a(A_c/A_p)^{\alpha} \qquad \text{(Eq. 23-31)}$$

where k_a and α are constants near unity, and A_c and A_p are the projected areas of the cluster (aggregate) and primary particle (monomer), respectively. Medalia (1967; Medalia, and Heckman 1969) first used this form and found empirically $k_a = 1.0$ and $\alpha = 1.1$. This has subsequently been corroborated by a number of workers with α varying by a few hundredths. Oh and Sorensen (1997) found that fractal soot clusters with $D_f \approx 1.75$ obeyed Equation 23-31 with $\alpha = 1.09$. Köylü et al. (1995) analyzed both computer-simulated and real soot clusters, and found $k_a = 1.15–1.16$ and $\alpha = 1.09–1.10$. Note that with these results the limit as $N \to 1$ is not preserved because k_a is not unity. In another simulation Meakin et al. (1989), created DLCA clusters with $D_f = 1.8$ and N up to $N = 10^4$, larger than any in any other work that

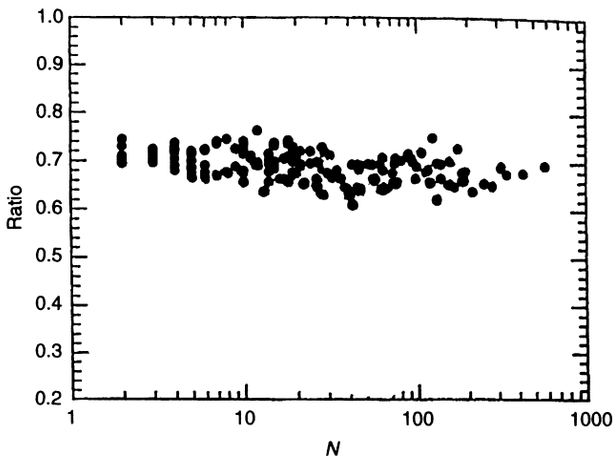

Figure 23-7 Ratio of the aggregate radius of gyration R_g (in $d = 3$ space) to half the longest length R_2 of the clusters projected onto a $d = 2$ plane as a function of N for simulated DLCA aggregates with $D_f = 1.79$.

has compared N to the projected area. They fit their data with

$$A_c/A_p = 0.4784N + 0.5218N^{0.7689} \qquad \text{(Eq. 23-32)}$$

This result is equivalent to Equation 23-31 with $k_a = 1.00$ and $\alpha = 1.10$ over the range of $N = 1-100$, $k_a = 1.00$ and $\alpha = 1.084$ for $N = 1-1000$, $k_a = 1.075$ and $\alpha = 1.083$ for $N = 10-100$, and $k_a = 1.106$ and $\alpha = 1.069$ for $N = 10-1000$. The slope of a log N versus log (A_c/A_p) graph is α, and Equation 23-32 yields a slowly decreasing α with increasing N. This is consistent with the notion that, for clusters with $D_f < 2$, as $N \to \infty$, N should be linear with A_c, that is, α asymptotically approaches 1.00, because the cluster dimension is less than the dimension of the plane onto which it is projected.

Brasil et al. (1999) studied this problem with the expressed interest to provide a recipe for image characterization of fractal-like aggregates. They found for DLCA-like aggregates $k_a = 1.10$ and $\alpha = 1.09$ for random projections, and $k_a = 0.97$ and $\alpha = 1.11$ for projections with the aggregate resting on three contact points on the projection plane. This latter projection seems reasonable to simulate the actual situation when aggregates are collected on a microscope grid. More recently Pierce et al. (2006) found exponents of about 1.08 with a small dependence on whether the aggregation was diffusive or ballistic.

In summary all these results agree fairly well, with typical differences a few percent but as large as 10% for the range $N = 10-1000$. Given this and because we desire to conclude with a recommendation, we recommend $k_a = 1.09$ and $\alpha = 1.08$. These yield N from the area ratio in good agreement, 5%, with all the values discussed above, and any fretting for more accuracy seems fruitless.

23.3.5.3 The Fractal Dimension There are three useful ways to determine the fractal dimension, D_f. Two methods analyze a single cluster; they are the method of nested circles or squares and the analysis of the density correlation function. The third method requires an ensemble of aggregates and compares N to R_g (or any measure of the aggregate's linear size) via Equation 23-16. We discuss these methods sequentially below.

23.3.5.3.1 The Method of Nested Circles or Squares In this method circles or squares of increasing radius or side length s are computer drawn on the aggregate centered on the aggregate's center of mass. The total binary dark or gray area G (arbitrary units) within the circle or square is calculated and plotted versus s. Then from Equation 23-18 the following scaling relation holds

$$G \approx s^{D_{f,2}} \qquad \text{(Eq. 23-33)}$$

Equation 23-33 is best used as a log-log plot of G versus s, which will have a slope of $D_{f,2}$. $D_{f,2}$ must be converted to the three-dimensional fractal dimension with Equation 23-25 and α.

Often a given cluster will yield a nonlinear, strangely shaped plot of N versus s. One must remember that "fractal" is a statistical concept and not all clusters are alike. Examination of an ensemble of clusters is therefore highly recommended. While most clusters will exhibit fractal behavior, that is, have a linear log G versus log s plot, occasional "odd" clusters will occur. An example of this cluster-to-cluster variation is given by Zhang et al. (1988) and reproduced in Figure 23-8. There it is found that the sum of the gray areas for three clusters is better described by Equation 23-33 than for any individual cluster. On the other hand, if there are more "odd" clusters than "fractals" then the system is not a fractal system.

23.3.5.3.2 The Density Correlation Method The density correlation function is a conditional probability that, given material at one point, defines the probability that there will be material at another. It is represented by $g(r)$ and is expressed by

$$g(r) = \langle \rho(R + r)\rho(R) \rangle \qquad \text{(Eq. 23-34)}$$

In Equation 23-34 $\rho(R)$ is the density at point R and the brackets $\langle \cdots \rangle$ mean an average over all positions R.

The digitized, binary images can be used to calculate $g(r)$. Since the density is proportional to the gray level of the

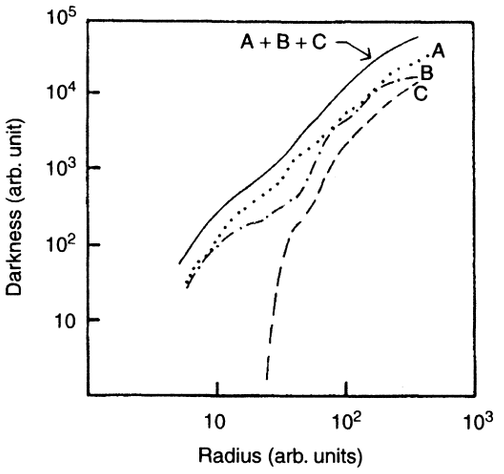

Figure 23-8 The total gray level (G_{tot} labeled "Darkness") within a series of nested circles centered on the cluster center of mass for three different soot clusters A, B, and C determined from their binary projected images. The curve $A + B + C$ is their sum, which is fairly linear to imply an average $D_f = 1.72 \pm 0.10$.

image, Equation 23-27, we can write Equation 23-34 as

$$g(r) = \sum_{u}^{N_u} \sum_{v}^{N_v} G(u+x)G(v+y)/N_u N_v \qquad \text{(Eq. 23-35)}$$

where

$$r = \sqrt{x^2 + y^2} \qquad \text{(Eq. 23-36)}$$

In calculating with Equation 23-35, u and v should be constrained to points (pixels) within the aggregate. This is not necessary, but otherwise $G = 0$ and unnecessary computation results. Note that Equation 23-35 could also be restricted to averages over u or v separately to yield $g(x)$ and $g(y)$. If these differed, anisotropy would be implied. Many different x and y values yield the same r, so these could be averaged over a range r to $r + dr$ to calculate a final $g(r)$.

Once the density correlation function is calculated, it can also be plotted on a log-log plot to display its power law nature, as written in Equation 23-17. If the projected image has been stored in the computer in a binary format, the projected image has pixels with gray level $G = 0$ or 1 only, and the effective spatial dimension is $d = 2$ to be used in Equation 23-17. Also for the binary format, the fractal dimension is $D_{f,2} = D_{f,3}/\alpha$, that is, the correction of Equation 23-25 must be made. Here again cluster to cluster variation is expected, but typically not as much as in the "nested" method above. Figure 23-9 gives an example for a soot fractal aggregate.

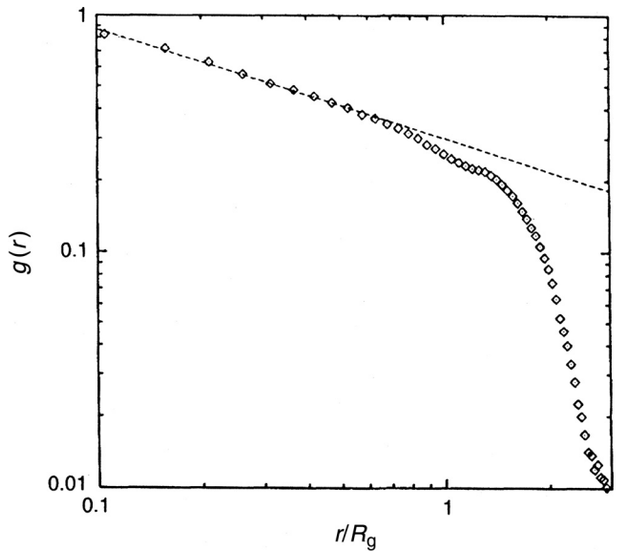

Figure 23-9 Density correlation function for a soot cluster obtained from a premixed CH_4/O_2 flame. Dashed line is a fit to the first 13 points [thereafter the cutoff fraction $h(x)$ takes over] of the power law $g(r) \sim r^{3\text{-D}}$.

23.3.5.3.3 The Ensemble Method Both N and R_g can be extracted from the projected, binary images of the fractal aggregates. Given these parameters, Equation 23-16 suggests that a log-log plot for a polydisperse ensemble of aggregates will yield D_f from the slope and k_o from the intercept. This fact has been used many times in the literature, and Figure 23-10 gives an example. Note that this analysis yields $D_f \equiv D_{f,3}$.

If k_o is not needed, this analysis can be simplified by using the total gray level of the binary projected image of the aggregate versus any aggregate length, for example, the longest, $2d$ projected length. The slope of such a graph would yield $D_{f,2}$. This method usually yields excellent results.

23.3.6 Aggregates with $D_f > 2$

Jullien et al. (1994), modeled $d = 3$ random fractal aggregates on a computer with $1 \leq D_f \leq 2.5$ and then studied their projection onto a plane. Figure 23-11 is a reproduction of their Figure 23-2a, which is particularly useful. It shows the binary projected fractal dimension $D_{f,2}$ versus the true, $d = 3$ fractal dimension D_f of the aggregate for a variety of aggregate sizes ranging from $N = 16-8192$. A line representing Equation 23-25 with $\alpha = 1.08$ is included. The data

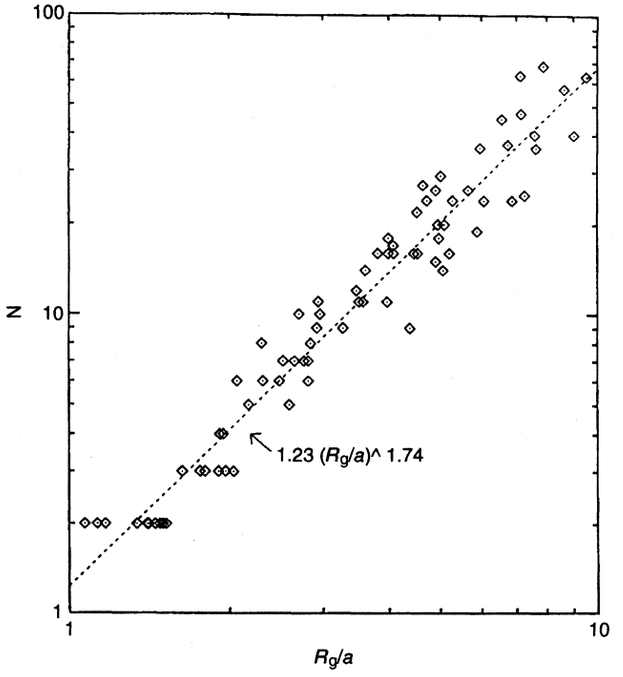

Figure 23-10 Total number of monomers per aggregate versus radius of gyration divided by the monomer radius for an ensemble of soot clusters collected from a premixed methane/oxygen flame. The slope of this log-log plot demonstrates the power-law dependency of Equation 23-16 and yields a fractal dimension of $D_f = 1.74 \pm 0.04$. The intercept yields $k_o = 1.23 \pm 0.07$.

for $D_f < 2$ support the line, giving yet more credence to that analysis.

For $D_f > 2$, however, this line fails, more so with increasing D_f. Jullien et al. (1994) also found from their computer simulations that, in the asymptotic limit of very large aggregates, the perimeter fractal dimension D_p is well defined and varies continuously with the mass fractal dimension of the three-dimensional aggregate. They proposed the following approximate formulas to account for this variation:

$$D_f = D_p, \qquad D_f < 2 \qquad \text{(Eq. 23-37)}$$

$$D_f = 3 - (D_p - 1)^{2/3}, \; D_f \geq 2 \qquad \text{(Eq. 23-38)}$$

We have confirmed the validity of these equations by measuring D_p for two-dimensional projections of computer-simulated clusters with known fractal dimensions (Dhaubhadel et al. 2006). To find D_p the number $N(L)$ of square meshes of size L, each of which includes at least one pixel of the fractal aggregate perimeter is determined when the digitized picture of the fractal aggregate is viewed under a grid. $N(L)$ and L are related to D_p as

$$N(L) = CL^{D_p} \qquad \text{(Eq. 23-39)}$$

where C is a constant of proportionality. The slope of a doubly logarithmic regression of $N(L)$ against L is D_p. This is illustrated in Figure 23-12. In the same work, Dhaubhadel et al. (2006) showed that the fractal dimension for any aggregate, regardless of whether $D < 2$ or $D > 2$, could be obtained by a structure factor analysis. For fractal aggregates, the structure factor $S(q)$ is given by (Sorensen 2001)

$$S(q) = 1, \qquad qR_g < 1 \qquad \text{(Eq. 23-40)}$$

$$= C(qR_g)^{-D}, \; qR_g > 1 \qquad \text{(Eq. 23-41)}$$

where q is the scattering wave vector, R_g is the radius of gyration of an aggregate, and C is a proportionality constant roughly equal to unity. $S(q)$ can be calculated for the digitized picture of the soot cluster using the formula

$$S(q) = N_{pix}^{-2} \left| \sum_{i=1}^{N_{pix}} e^{i\vec{q}\cdot\vec{r}_i} \right|^2 \qquad \text{(Eq. 23-42)}$$

where N_{pix} is the total number of dark pixel points in the picture and $\vec{r}_i$ is the position vector of the ith dark pixel. Dhaubhadel et al. (2006) showed that the resulting $S(q)$ had many rather random "interference" wiggles, but the envelope functionality was a power law at large qR_g as described by Equation 23-41. Figure 23-12 shows that this structure factor analysis and the perimeter analysis yield consistent results for a large $D_f = 2.46 \pm 0.04$ fractal aggregate.

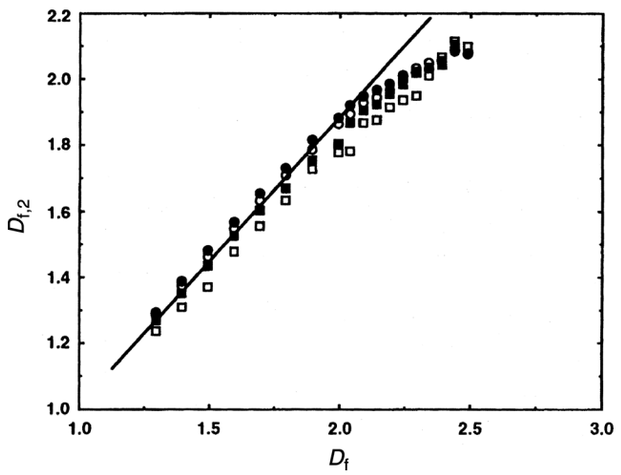

Figure 23-11 Fractal dimension $D_{f,2}$ of the projection of a fractal aggregate versus its $d = 3$ space fractal dimension, D_f, for $N = 16$ (open circles), 128 (filled circles), 1024 (open squares), 8192 (filled circles) for computer-simulated aggregates (after Jullien et al. [1994]). Line is Equation 23-25 with $\alpha = 1.08$.

23.3.7 Fractal Aggregate Mobility and Dynamic Shape Factor

In this section we restrict our discussion to diffusion limited cluster aggregates, DLCA, with a fractal dimension of $\approx$1.78, since nearly all research regarding mobility has concerned these common aggregates. One can find, however, references to larger fractal dimension aggregates ranging from 2.1 to 2.4 in the aerosol literature. These values, however, are very likely erroneous interpretation of the scaling relation between the mass and mobility size and cannot be considered true fractal dimensions. Indeed, these aggregates are very likely DLCA. Some comment to that is given below during the discussion of the small N limit.

Sorensen and co-workers (Cai and Sorensen 1994; Wang and Sorensen 1999) have used light scattering to study fractal aggregate diffusivity. This is relevant to the mobility and dynamic shape factor because the diffusion coefficient D and the coefficient of the drag force f in $F_D = f\,V$, where V is the particle velocity, are related by the Einstein relation

$$D = kT/f \qquad \text{(Eq. 23-43)}$$

Here k is the Boltzmann constant and T is the temperature. Their method used static light scattering to measure the aggregate radius of gyration, R_g, and the fractal dimension D_f, and dynamic light scattering to measure the diffusion coefficient D. The fractal aggregates were soot in a premixed methane/oxygen flame and TiO_2 aggregates in air at room temperature and pressures from 1/15 to 1 atmosphere. Wang and

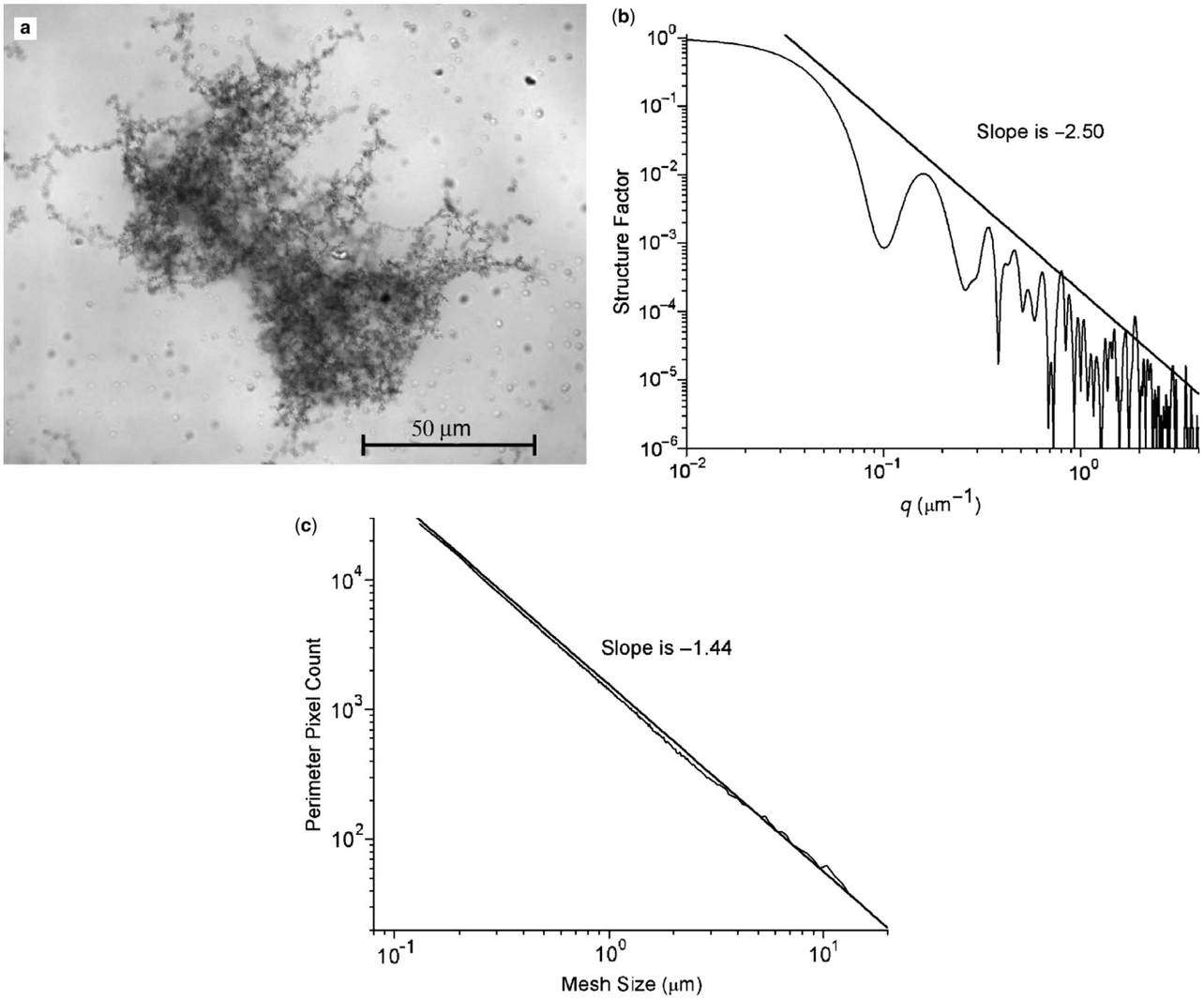

Figure 23-12 **(a)** Transmission electron microscope picture of a large soot cluster (note the scale bar) and **(b)** structure factor of and **(c)** perimeter analyses of part (a). The fractal dimension is equal to the slope in the structure factor analysis. The perimeter analysis slope yields the perimeter fractal dimension, 1.44. The mass fractal dimension is found via Equation 23-38 to be 2.42.

Sorensen also reinterpreted aerosol mobility data of Schmidt-Ott (1988) and Rogak et al. (1993) and the colloidal data of Wiltzius (1987), and combined all these with their data to achieve a general picture of the mobility of fractal aggregates at all values of the Knudsen number. Subsequently, other workers have considered the problem of fractal aggregate mobility and all these efforts yield the description below.

There are four regimes that must be delineated to understand the mobility of a fractal aggregate. These four regimes are due to the combination of the following two size classifications:

1. The aggregate mobility radius, R_{mob} $(= d_{\text{B}}/2)$, will have different functionalities on the primary particle (or monomer) number N, depending on whether N is either less or greater than a certain critical number, N_{c}. This classification results from the need for the aggregate mobility to have the correct small N behavior and limit at $N = 1$, where R_{mob} must equal a, the primary particle radius.
2. R_{mob} will have different functionalities on N, depending on the Knudsen number, Kn. For fractal aggregates Kn could be calculated using either the radius of gyration, R_{g}, or R_{mob}, or some other linear measure. This issue is not yet resolved.

The need for the proper behavior of R_{mob} in the $N = 1$ limit becomes evident when one considers experimental (Wiltzius

1987; Wang and Sorensen 1999) and theoretical (Kirkwood and Riseman 1948; Meakin et al. 1985) results in the continuum regime. There, one finds $R_{mob} = \beta R_g$ with $\beta = 0.75 \pm 0.05$ for large fractal aggregates ($N \gg 1$). Note, however, at $N = 1$, $R_g = \sqrt{\frac{3}{5}} R$ for a spherical primary particle (of radius R) and since $R = R_{mob}$ for a sphere, then $\beta = 1.29$ at $N = 1$. The implication is that $\beta = R_{mob}/R_g = 0.75$ at large N must at some point, call it N_c the "crossover N," change its constancy with size and evolve with decreasing N from 0.75 to 1.29 at $N = 1$. This behavior was seen by Wang and Sorensen when they reanalyzed the data of Cai and Sorensen (1994) with Knudsen numbers of ca. 6.7 to 22, Schmidt-Ott (1988) with Knudsen numbers of ca. 1.3 to 7, and Rogak et al. (1993) with Knudsen numbers of ca. 0.1 to 2. All three data sets followed a power law functionality $R_{mob} = aN^x$ with exponents $x = 0.43$, 0.46, and 0.45, respectively, as they approached the $N = 1$ limit. Chan and Dahneke (1981) calculated the drag force on linear aggregates in the free molecular regime. For small N their results limit properly to $N = 1$ and display the same power law with an exponent of $x = 0.45$ for $N = 1$ to 10. Given these data and implications, Wang and Sorensen proposed that the approach to the $N = 1$ limit was the same regardless of the Knudsen number and is described by

$$R_{mob} = aN^{0.45}, \quad N < N_c \qquad \text{(Eq. 23-44)}$$

Recently Cho et al. (2007) reported measurements for aggregates with $N = 3$, 4, and 5, and Knudsen numbers in the range of 0.3 to 0.7. Our analysis of their data agrees with Equation 23-44 with an exponent of $x = 0.44$. Similarly, recent data reported by Shin et al. (2009, 2010) also agrees with our analysis. Moreover, there are numerous reports of how aggregate mass scales with R_{mob} with a "fractal dimension" of anywhere between 2.1 to 2.4. In all these reports the aggregates are small enough such that $N < N_c$. The true fractal dimension is very likely ca. 1.8 and the observed functionality is the crossover functionality of Equation 23-44, consistent with the inverse of those "fractal dimensions," 0.48 to 0.42.

23.3.7.1 Fractal Aggregate Mobility in the Continuum Regime Experiments (Wiltzius 1987; Wang and Sorensen 1999; Gwaze et al. 2006) and theory (Kirkwood and Riseman 1948; Meakin et al. 1985) give a consistent picture for the continuum limit with $N > N_c$ that

$$R_{mob} = \beta R_g \qquad \text{(Eq. 23-45)}$$

$$\beta = 0.75 \pm 0.05 \qquad \text{(Eq. 23-46)}$$

Use of Equation 23-16 yields

$$R_{mob} = a\beta k_0^{(-1/D_f)} N_f^{(1/D_f)} \qquad \text{(Eq. 23-47)}$$

The numerical value of the coefficient in Equation 23-47 is uncertain due to the uncertainty of its parameters. In our opinion the best values for these parameters are: $\beta = 0.75$, $k_0 = 1.4$, $D_f = 1.78$. This yields

$$R_{mob} = 0.62aN^{0.56} \qquad \text{(Eq. 23-48)}$$

23.3.7.2 Fractal Aggregate Mobility in the Free Molecular Regime There are a number of results that yield a consistent description of fractal aggregate mobility in the free molecular regime. Wang and Sorensen concluded that $R_{mob} = aN^{0.46}$ in this regime. It is expected that the drag is proportional to the effective projected area of the aggregate accounting for screening of monomers by other monomers during projections. Thus Wang and Sorensen (1999) concluded that the results of Meakin et al. (1989) implied $R_{mob} = aN^{0.46}$ (see the discussion above). Recent simulation results obtained by Pierce at al. (2006), yield the same conclusion. Recently, Mackowski (2006) performed a definitive simulation to resolve this problem and found $R_{mob} = 0.9aN^{0.47}$.

Given all these results, we recommend

$$R_{mob} = aN^{0.46}, \quad N > N_c \qquad \text{(Eq. 23-49)}$$

This is remarkably close, certainly within error, to the result for $N < N_c$ and thus one could claim that there is no crossover. Such a claim would be misleading because the physics for the two regimes is different.

The value for N_c is obtained from the continuum results, Equations 23-45 and 23-47. We find

$$N_c = [\beta/k_0]_f^{1/(Dx-1)}$$

The numerical value of N_c ranges widely due to the uncertainties in its parameters. In our opinion the best values for these parameters are: $\beta = 0.75$, $k_0 = 1.4$, $D_f = 1.78$ and $x = 0.45$. These yield

$$N_c = 70 \qquad \text{(Eq. 23-50)}$$

In summary, the mobility radius of a DLCA fractal aggregate with $D_f = 1.78$ is given by the following matrix:

Mobility Radius, R_{mob}, for DCLA Fractal Aggregates

Flow regime	$N < N_c$	$N > N_c$
Continuum	$aN^{0.45}$	$0.62aN^{0.56}$
Free molecular	$aN^{0.45}$	$aN^{0.46}$

To recast the mobility radius results into the dynamic shape factor, recognize that Equation 23-5 implies for the continuum regime

$$\chi = R_{mob}/R_v \qquad \text{(Eq. 23-51)}$$

and

$$\chi = (R_{mob}/R_v)^2 \qquad \text{(Eq. 23-52)}$$

in the free molecular regime where R_v is the volume equivalent radius ($= d_v/2$). We have $R_v = aN^{1/3}$. One can then recast the mobility radius matrix into a dynamic shape factor matrix:

Dynamic Shape Factor, χ, for DLCA Fractal Aggregates

Flow regime	$N < N_c$	$N > N_c$
Continuum	$N^{0.12}$	$0.62N^{0.23}$
Free molecular	$N^{0.24}$	$N^{0.26}$

23.4 FIBERS

23.4.1 Introduction

The term "fiber" has been applied to a wide variety of nonspherical particles having an elongated shape, that is, one particle dimension significantly greater than the other two. Airborne fibers generally are of microscopic dimensions, typically less than 100 μm in their longest dimension and less than 10 μm in their shortest dimension. Airborne fibers may also consist of bundles of thinner fibers. Except in the case of certain engineered nanomaterials, such as carbon nanotubes and nanofibers, most fibers of microscopic dimensions tend to be incidental byproducts of the manufacturing and processing of materials that are fibrous on the macroscopic scale. Certain nonfibrous materials can produce fibers when subject to stress. Certain fibers have several unique properties that make them useful from a commercial standpoint. Asbestos, for instance, includes six commercial fibrous minerals that have high tensile strength, chemical resistance, and excellent thermal and acoustic insulation characteristics. These properties have made asbestos useful in a variety of products, including friction materials, high temperature insulating materials, acoustic insulation, fireproof cloth and rope, and floor tiles. Besides asbestos, other mineral fibers exist in nature. Several materials, including glass and mineral slags, have been melted and spun into fibers. Ceramic materials have similarly been spun into fibers, as well as grown by chemical and vapor crystallization. Carbon and graphite fibers are produced commercially for high strength products. Organic fibers, such as cotton, wood, and other cellulosic materials are widely present in the environment, both from commercially produced materials as well as natural sources. Carbon nanotubes are a tubular form of carbon "buckyballs" (C_{60}), a molecular structure of pure carbon with very high strength and high conductivity (Ren et al. 1998). These nanotubes are being commercially developed for variety of applications. Besides cylindrical particles that have relatively high strength, chains of particles also may behave as fibers and can serve as models for some aerodynamic properties of fibers. Some organic materials can be crystallized into well-defined fibrous shapes and can be used to test theories of fiber aerodynamic behavior.

Asbestos fiber aerosols have been closely associated with several diseases of the respiratory system (National Institute for Occupational Safety and Health, 1976). Thus, the fibers that can enter the respiratory system are of greatest concern. The seriousness of the diseases has driven measurement technology to provide maximum sensitivity and accuracy for measuring asbestos aerosols. Other airborne fibers may have one or more of the same physical and chemical properties as asbestos. In some cases, human exposures and/or animal studies suggest the disease potential of these fibers. Thus, there is concern regarding the health effects of fibers other than asbestos.

The dimensions of fibers in aerosols can cover a wide range. Asbestos consists of material composed of individual fibrils as small as 0.025 μm (Langer et al. 1974). Airborne fibers can be single fibrils or various-sized bundles with a range of diameters, while lengths can be less than 0.5 μm to several hundred micrometers. The dimension distributions depend on the fiber type as well as how the fibers were comminuted from the bulk material. The magnitude of disparity between length and diameter often makes it difficult to make accurate size distribution measurements. Several protocols, using various types of microscopes, have been developed to deal with fiber distribution measurement. Other types of instruments, primarily using light-scattering properties, have been developed to characterize fibers. However, these instruments usually provide only an approximate indication of fiber dimensions.

Note that the following discussion, except where otherwise indicated, will deal largely with measurement of aerosolized fibers, generally visible only with a microscope, and not with the macroscopic or bulk properties of the fibrous material. Since asbestos has been the most intensely studied type of fiber, many comments will relate to this material. Many issues regarding asbestos mineralogy, health effects, and measurement techniques are discussed in reviews by Langer (1974), Walton (1982), and Dement (1990). Additional topics are presented in books by Selikoff and Hammond (1979), Rahjans and Sullivan (1981), Michaels and Chissick (1979), Chissick and Derricott (1983), and Holt (1987). Similar reviews have been carried out for man-made fibers (NIOSH 1976, 1977; International Agency for Research on Cancer [IARC] 1988).

23.4.2 Fiber Shape

The behavior of fibers suspended in a gas is a function of the fiber dimensions. Assuming either a cylindrical or prolate spheroidal shape, these dimensions can be defined by two parameters, length and diameter. A third parameter β_a is often invoked to indicate the fibrosity or aspect ratio, that is, the ratio of the length to the diameter. However, real fibers frequently do not meet the either the ideal cylindrical or the prolate spheroid shape assumption. Glass or mineral

fibers are often nearly cylindrical, but even these fibers frequently display curvature along their length as well as bulbous or jagged ends. Asbestos fibers are formed from a unique crystal habitat in which the bulk mineral has slip planes in two directions, but only rarely in the third. This results in a propensity to produce particles that can split longitudinally to produce thinner and thinner fibers, ultimately resulting in fibrils about 0.02- to 0.05-μm diameter. Thus, while some asbestos fibers exhibit a nearly ideal cylindrical shape, others may have various combinations and degrees of splayed ends, curvature, splitting, noncircular circumference, and so on. For instance, the magnetically aligned chrysotile fibers in Figure 23-13 show many of these characteristics. In spite of these possible variations in shape, fibers are still most often characterized simply by length and diameter.

Distributions of natural fibers are rarely monodisperse in diameter and even more rarely so in length. This has made it difficult to provide adequate calibration for instruments that attempt to measure fibers as well as to perform measurements of fiber toxicity as a function of fiber dimension. Distributions of fibers can often be described by a two-dimensional (length l and diameter d_f) lognormal distribution (Schneider et al. 1983; Cheng 1986), that is, ln l and ln d_f are each distributed normally. The probability density function is given by

$$f(l, d_f) = \frac{1}{2\pi\sigma_{df}\sigma_l\sqrt{1-\tau^2}ld_f} \exp\left(-\frac{A^2 + B^2 - 2\tau AB}{2(1-\tau^2)}\right) \quad \text{(Eq. 23-53)}$$

where $A = (\ln d_f - \mu_{df})/\sigma_{df}$, and $B = (\ln l - \mu_l)/\sigma_l$, μ_i and σ_i^2 are the mean and variance of the natural logarithm of l and d_f, respectively, and τ is the correlation between ln l and ln d_f. The five parameters μ_l, μ_{df}, σ_l, σ_{df}, and τ are needed to define completely a two-dimensional size distribution. The two-dimensional lognormal size distribution has the properties that the marginal and the conditional distributions are lognormal (Holst and Schneider 1985). The former property indicates that the length and diameter distributions are each separately lognormal. The latter indicates that functions of length and diameter of the form $kd_f^p l^q$, where k, p, and q are constants, are also lognormal. Such functions include aspect ratio, surface area, volume, and aerodynamic diameter. Deviations from lognormality can sometimes be attributed to artifacts in sampling or analysis or to multiple aerosol generation sources.

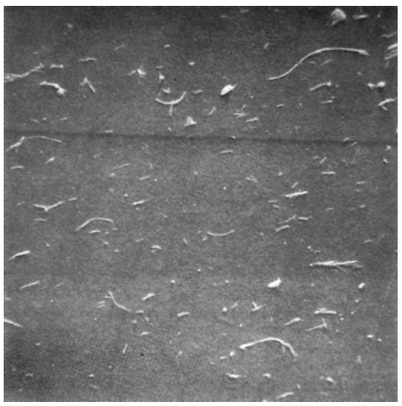

Figure 23-13 Scanning electron micrograph (1500×) of an aqueous sample of magnetically aligned UICC Canadian chrysotile collected on a 0.1-μm pore size filter. Reprinted from Timbrell (1973) with permission.

Many fiber distributions reported in the literature include the length and diameter means and variances, but unfortunately do not include τ. However, if the original data is reported in a table as a function of both length and diameter the correlation term can be estimated (Cheng 1986). Most fiber distributions have positive τ, suggesting that diameter often increases with length.

There have been measurements of a variety of fibrous aerosols. Table 23-3 lists the results of some examples. Some of these materials have been generated for toxicity studies; some have been measured in environmental studies, while others have been generated as calibration materials. It is necessary to exercise caution when comparing fiber size distributions from different analytical procedures. A comparison of concentrations of asbestos fibers >5 μm in length by optical and electron microscope (Dement and Wallingford 1990) showed a good correlation ($R^2 = 0.87$) but with a bias towards greater numbers of fibers under the electron microscope (slope of 1.07), thought due to the difference in resolution of thin fibers (less than approximately 0.2-μm thick). The ability of the optical phase-contrast microscope to resolve fibers is a function of the difference in refractive index between the object and the surrounding medium. Given a microscope appropriately set up for fiber counting, chrysotile fibers down to a width of 0.15 μm could be observed under green light against a background of Euparal™ medium, with a refractive index of 1.48 (Rooker et al. 1982). Smaller diameters of amphibole fibers, which have a higher refractive index than chrysotile, should be visible, especially against Triacetin™ medium, which has a lower refractive index of 1.43. Amphibole asbestos fibers are usually also wider than chrysotile fibers, so that while optical microscope counts of chrysotile may underestimate fibers compared to the electron microscope, amphibole asbestos counts by the optical microscope may approach the true number.

The Dement and Wallingford study also noted the majority of airborne fibers were <5-μm long, and that there was a much greater variability between the optical and electron microscope determinations of the concentration of all fibers. It was noted in a recent study that fibers shorter than 2–3 μm are often not recognized as fibers under the optical microscope (Harper et al. 2008). In addition, the

TABLE 23-3 Examples of Measured Fiber Site Distributions

Material	Diameter (μm)	σ_g	Length (μm)	σ_g	MMAD (μm)	σ_g	Measurement Technique
Chromoglycic acid[a]	0.205	1.58	2.09	1.83			SEM
					0.65	1.88	Cascade impactor
Sugar cane silicate[b]	0.3–1.5[j]		3.5–65[j]				TEM
Caffeine[c]	1.13	1.08	5.55	1.12			SEM
					2.1	1.1	Sedimentation
Ceramic fibers[d]							
Sample a	0.5		10.1				TEM
Sample b	0.66		8.3				TEM
Sample c	0.98		22.8				TEM
Chrysotile[e]							
Preform ring	0.13	2.15	1.6	2.7			TEM
Yarn dressing	0.08	1.92	1.0	2.4			TEM
Cure press	0.13	1.94	1.5	2.2			TEM
Crocidolite[f]							
Mine/mill[g]	0.08–0.10	1.86–2.08	0.98–1.25	2.30–2.55			TEM
Manufacturing	0.04	1.58	0.54	2.32			TEM
Fibrous glass[h]							
Code 100	0.12	1.8[k]	2.7	2.2[k]			TEM
Code 110	1.8	1.7[k]	26	2.0[k]			TEM
Iron oxide chains[i]							
	0.059	1.1	1[l]	2.0			TEM
					0.32	1.11	Centrifuge

[a]Chan and Gonda (1989).
[b]Boeniger et al. (1988).
[c]Vaughan (1990).
[d]Rood (1988).
[e]Pinkerton et al. (1983).
[f]Hwang and Gibbs (1981).
[g]These values represent the range of several measurements that produced similar results.
[h]Timbrell (1974).
[i]Kaspar and Shaw (1983).
[j]These values represent the range of particle sizes rather than the median diameters.
[k]Estimated from data in reference.
[l]Estimated from mean chain length of 22 primary particles.

smaller field of the electron microscope also contributes towards differences. Attempts to measure "optical equivalent" distributions for asbestos fibers from observations using an electron microscope often fall short of their goal, which is why the NIOSH 7402 method (NIOSH 1994b) only uses the optical equivalent (PCM-equivalent, or PCMe) count to calculate the percentage of fibers that are asbestos and then that percentage is applied to a separate PCM count. Finally, it should be noted that most microscopic techniques give little information about the third dimension (although tilting the stage, or examining shadows is possible in some instances). Thus, some platy materials, such as talc, can be mistakenly observed as fibers when they are on edge.

23.4.3 Fiber Behavior

23.4.3.1 Translational Motion As noted earlier, transport behavior of fibers depends on whether the major axis is oriented parallel to or perpendicular to the direction of the motion relative to the surrounding gas (Fig. 23-14a,b). The drag on a fiber is greatest when it is oriented perpendicular to the flow of the surrounding gas. Fiber behavior is often described in terms of a combination of the two orientations. While the difference in drag between the two orientations is typically about 15–30%, it can be difficult to determine the contribution of each orientation in experimental systems. At low Reynolds number (Re_p), fiber orientation will be stable (discounting Brownian rotation) and will not change due to translational motion, for example, during gravitational settling (Gallily 1971). In addition, fibers settling in still air will not settle exactly in the direction of the gravitational force, but will drift somewhat due to orientation (Weiss et al. 1978). Larger fibers, with Re_p greater than about 0.01, will settle with their major axis oriented perpendicular to the direction of motion (Fig. 23-14a). With increasing Re_p ($Re_p > 100$), longer fibers ($\beta_a > 20$) are still stable in the

perpendicular orientation, but there is an increasing trend toward instability (Clift et al. 1978).

The aerodynamic diameter d_a of a prolate spheroid is given by (Fuchs 1964),

$$d_a = d_f \sqrt{\frac{\rho_f \beta_a}{\rho_0 \chi}} \qquad \text{(Eq. 23-54)}$$

where, d_f is the physical fiber diameter, ρ_f is the fiber density and ρ_0 is standard density. A cylinder with the same diameter and length as a prolate ellipsoid has $3/2$ greater volume and mass. Therefore, for cylinders with the same axial dimensions, the right-hand side of Equation 23-54 must be multiplied by $(3/2)^{1/3}$ or $(3/2)^{1/2}$ to obtain the equivalent-volume or equivalent-mass diameter, respectively (Griffiths and Vaughan 1986). For motion perpendicular (Fig. 23-14a), and parallel (Fig. 23-14b) to the fiber major axis, the respective dynamic shape factors $\chi_\parallel$ and $\chi_\perp$ are given by Fuchs (1964),

$$\chi_\parallel = \frac{4(\beta_a^2 - 1)}{3} \Bigg/ \left\{ \beta^{1/3} \frac{2\beta_a^2 - 1}{\sqrt{\beta_a^2 - 1}} \ln\left(\beta_a + \sqrt{\beta_a^2 - 1}\right) - \beta_a^{4/3} \right\} \qquad \text{(Eq. 23-55)}$$

$$\chi_\perp = \frac{8(\beta_a^2 - 1)}{3} \Bigg/ \left\{ \beta_a^{1/3} \frac{2\beta_a^2 - 3}{\sqrt{\beta_a^2 - 1}} \ln\left(\beta_a + \sqrt{\beta_a^2 - 1}\right) + \beta_a^{4/3} \right\} \qquad \text{(Eq. 23-56)}$$

An alternate approach for directly calculating the aerodynamic diameter of cylinders (Cox 1970) gives similar results

$$d_{a,\parallel} = d_f \sqrt{\frac{9\rho_f}{4\rho_0}(\ln(2\beta_a) - 0.807)} \qquad \text{(Eq. 23-57)}$$

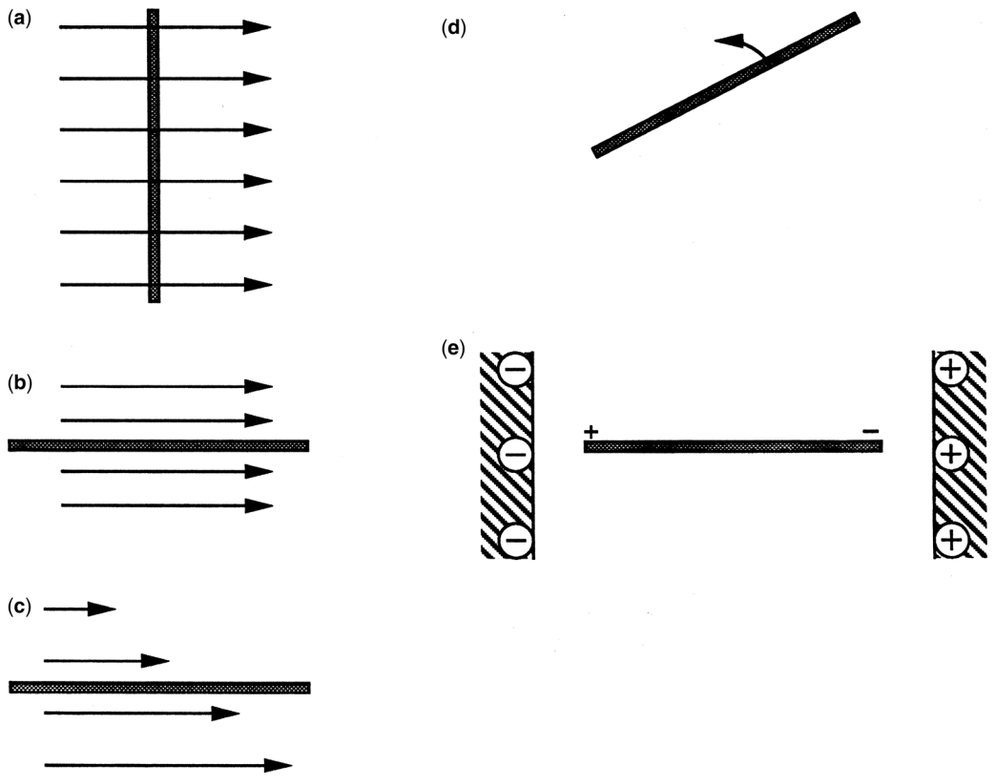

Figure 23-14 Fiber alignment in various force fields. **(a)** Fiber aligned perpendicular to relative gas motion. This is the preferred orientation during gravitational settling and acceleration at $0.01 < Re < 100$ in absence of other forces. **(b)** Fiber parallel to relative gas motion. Fiber motion is often treated as a combination of cases (a) and (b). **(c)** Fiber is readily oriented parallel to, or at some small angle to, the direction of shear flow in the suspending gas medium. **(d)** Small fibers governed by diffusional forces may exhibit completely random orientation. **(e)** Conductive fibers are aligned parallel to an electric field. Many fibers are also aligned in a magnetic field, usually parallel to the field lines, though they may be aligned perpendicular to the field or, for some materials, at some intermediate angle.

and

$$d_{a,\perp} = d_f \sqrt{\frac{9\,\rho_f}{8\,\rho_0}(\ln(2\,\beta_a) + 0.193)} \qquad \text{(Eq. 23-58)}$$

If fibers are not preferentially oriented by a drag force or other alignment force, the orientation may be completely random. Then, a single, orientation-averaged dynamic shape factor can be calculated using Equation 23-7.

In the presence of velocity gradients, the fiber will experience a torque until the fiber is oriented parallel to the direction of shear force (Fig. 23-14c). Thus, a fiber settling in a horizontal laminar flow will tend to be oriented horizontally (parallel to the shear force). However, the fiber will experience a periodic instability and perform a "flip." This instability is a function of fiber dimensions as well as the velocity gradients. Under such conditions, the aerodynamic diameter is not strictly an inherent property of the particle and depends on the experimental conditions of measurement (Gallily and Eisner 1979).

Inertial separation is commonly used for particle separation and sizing, for example, in impactors and cyclones. In such systems where flow conditions are rapidly changing, the fiber mechanics are governed by initial orientation and flow relaxation time besides the usual parameters observed for spherical particles (Gallily et al. 1986). For instance, fibers with large rotational inertia (especially long fibers) may not orient completely or may over-rotate in passing through a nozzle. Fiber behavior under such conditions may be only approximately characterized using Stokes number or other nondimensional parameters.

Experimental measurement of fiber deposition has been carried out in horizontal elutriators (Gallily and Eisner 1979; Griffiths and Vaughan 1986; Iles 1990), centrifuges (Stöber et al. 1970; Martonen and Johnson 1990; Asgharian and Godo 1999), impactors (Burke and Esmen 1978; Prodi et al. 1982; Asgharian et al. 1997), and cyclones (Fairchild et al. 1976; Iles 1990) for a variety of fiber types.

The extended shape also means that interception during translational motion plays a larger role in fiber deposition than for compact particles. However, the alignment of fibers by shear flow often reduces the effect of length on interception.

23.4.3.2 Rotational Motion The rotational mobility B_r of a high-aspect ratio ellipsoid can be approximated by (Lilienfeld 1985)

$$B_r = \frac{3(2\ln(2\,\beta_a - 1))}{2\pi\mu L^3} \qquad \text{(Eq. 23-59)}$$

where μ is the viscosity of the gas. Note that the rotational mobility is a strong inverse function of fiber length. Similarly the rotational diffusion coefficient D_r for fibers is also a strong function of fiber length

$$D_r = \frac{3kT}{\pi\mu\beta L^3}(\ln 2\,\beta_a - \delta) \qquad \text{(Eq. 23-60)}$$

where k is the Boltzmann constant, T is temperature, and δ is 1.4 for aspect ratios β_a larger than 10. Rotational mobility can be estimated by measuring the rate of relaxation after removal of an electrostatic alignment force (Cheng et al. 1991).

23.4.3.3 Behavior in the Transition Regime Under molecular bombardment, fibers can exhibit both rotational diffusion as well as translational diffusion. Such fibers are likely to be randomly oriented (Fig. 23-14d). As for fibers in the Stokes regime, it is often convenient to separate the translational motion of fibers into motion in which the major axis is parallel to the direction of motion and another in which the major axis is perpendicular to the translational motion. Diffusion of fibers is described by the diffusion coefficient D_{fib} (m^2/s)

$$D_{fib} = BkT = \frac{kT}{f} = \frac{kTC_{fib}}{f^\circ} \qquad \text{(Eq. 23-61)}$$

where B is the fiber's mechanical mobility (dyne-cm/s) and f° is the drag per unit velocity of the fiber in the continuum regime, f is the drag per unit velocity of the fiber corrected for slip by the fiber slip correction factor C_{fib}, and can be calculated using the adjusted sphere approach discussed earlier (Dahneke 1973a,b,c).

Fiber diffusional behavior is usually treated as a modification of spherical particle diffusion using particle shape factors (Asgharian and Yu 1988). This approach has agreed well with experimental diffusion coefficient measurement of fibers with mean diameters between 0.24 to 0.38 μm (Gentry et al. 1983). Diffusional coefficients of much smaller fibers have also been measured (Gentry et al. 1988) that show higher diffusion coefficients than expected.

As with the stagnant flow conditions for fibers in the continuum regime, fibers are expected to be randomly oriented unless affected by shear or other forces. Again, the longer the fiber, the more likely it is to be oriented by such forces.

Several studies have estimated effects of various deposition mechanisms (diffusion, impaction, interception) to determine overall particle deposition in filters (Fu et al. 1990) and lung airways (Asgharian and Yu 1989; Balásházy et al. 1990; Asgharian et al. 1997).

23.4.3.4 Charging Theories for unipolar diffusion charging (Laframboise and Chang 1977) and bipolar diffusion charging (Wen et al. 1984) of fibers have been developed. Unipolar charging of fibers causes the charge of long, thin fibers to increase significantly, though the electrical mobility changes relatively slowly with aspect ratio (Yu et al. 1987).

Such a variation of mobility with fiber aspect ratio may allow separation of fibers of different lengths.

23.4.3.5 Electric Field Effects A fiber may be aligned in an electric field by an induced dipole in the fiber. This requires that charges in the fiber be separated so that the polarity is opposite to that of the surrounding electric field as shown in Figure 23-14e. The charge separation from conduction is usually greater than that from polarization of the material. For charge separation to occur, the fiber must be sufficiently conductive so that the charges can migrate the length of the fiber in a reasonable time. Aerosol particles, even those consisting of a normally nonconducting material, can often be considered conductive because of their low capacitance and small dimensions (Fuchs 1964; Lilienfeld 1985). Surface impurities can also contribute to a particle's conductivity. In addition, water adsorbed on the fiber surface (e.g. glass fibers at ~50% relative humidity) can increase the conductivity and allow fiber alignment in an electric field. Thus, an electric field of sufficient strength ($1 \times 10^5 - 5 \times 10^5$ V/m) can overcome diffusional randomization and shear forces to align most types of fibers, including relatively nonconductive ones. For instance, electrostatically aligned zinc oxide fibers were used to modulate microwave radiation (Tolles et al. 1974).

When fibers and compact particles of the same aerodynamic diameter are charged under the same conditions, the fibers may have higher mobility than compact particles. Field studies of work environments suggested that fibers carried a charge proportional to fiber length (Johnston et al. 1985). Other studies indicated that unipolar, charged particles can be separated according to aspect ratio (Griffiths et al. 1985; Yu et al. 1987).

Electrostatic enhancement of fiber deposition in lungs (conductive tubing) has been observed (Jones et al. 1983). Calculations support such enhancement of sedimenting charged fibers (Chen and Yu 1990).

23.4.3.6 Dielectrophoresis Dielectrophoresis was investigated for separating aluminum wires of different lengths in liquid suspension (Lipowicz and Yeh 1989). Baron demonstrated that fiber length classification could be achieved for fibers as short as 4 μm in a 0.76-m long classifier (Baron et al.1994). This technique has been used for production of small quantities of classified fibers for *in vitro* cell assay studies and for fiber size measurement (Baron et al. 1998; Ye et al. 1999).

23.4.3.7 Magnetic Field Effects If a suspension of fibers in a liquid or gas is subjected to a magnetic field, fibers with sufficient magnetic susceptibility will align at some angle to the field. Usually this angle is either 0° or 90°; some amphibole asbestos samples have fibers aligned at both angles. Timbrell (1975) developed a technique for preparing permanently aligned samples by allowing a suspension of fibers in 0.5% celloidin/amyl acetate to dry in a 5–10,000 gauss magnetic field. Several fiber types have been aligned by Timbrell (1972, 1973), including carbon fibers and the various types of asbestos. Fibers of glass, silicon carbide, silicon nitride, and tungsten-cored boron did not align in similar fields.

Figures 23-15, 23-16, and 23-17 contain images of fibers magnetically aligned on a slide surface with light-scattering

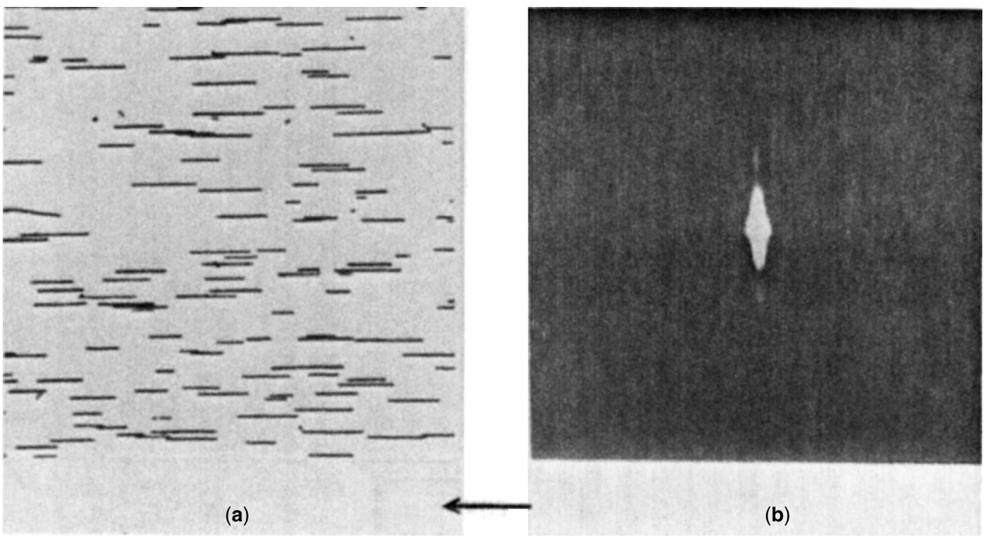

Figure 23-15 **(a)** Phase contrast microscope image of magnetically aligned carbon fibers suspended in celloidin on a glass slide. **(b)** Light-scattering pattern from the same fibers in aqueous suspension. The direction of the magnetic field is indicated by the arrow. Note the monodisperse diameter of the fibers, reflected in the sharply defined scattering pattern. Reprinted from Timbrell (1973) with permission.

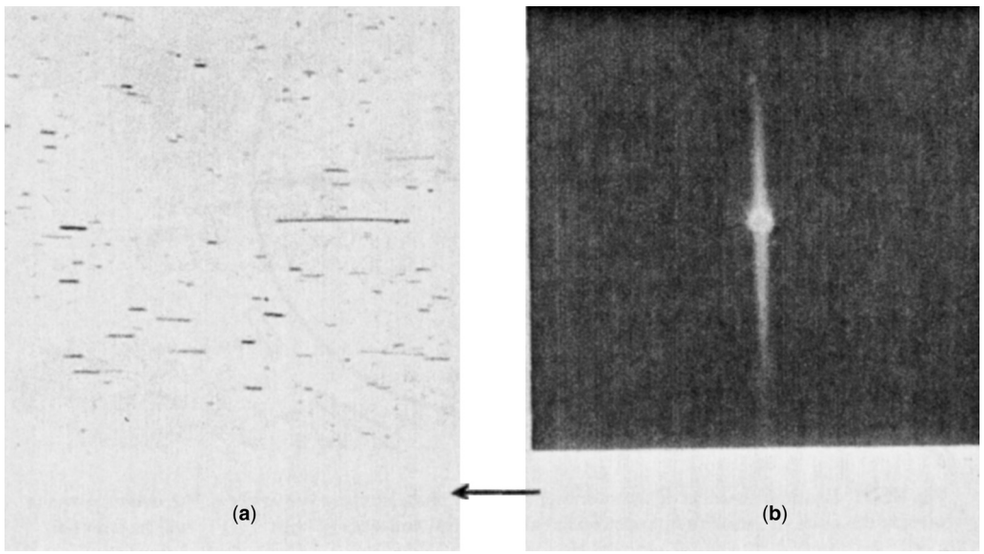

Figure 23-16 **(a)** PCM image of magnetically aligned UICC crocidolite fibers suspended in celloidin on a glass slide. **(b)** Light-scattering pattern from the same fibers in aqueous suspension. The direction of the magnetic field is indicated by the arrow. Reprinted from Timbrell (1973) with permission.

patterns from magnetically aligned liquid suspensions of the same types of fibers. The direction of the magnetic field is shown in the figures. The scattering pattern has the main laser beam in the center, with the plane of scattering radiating in opposite directions. In Figure 23-15, monodisperse diameter carbon fibers all are aligned parallel to the field so that a well-defined scattering pattern perpendicular to the field is produced. The crocidolite fibers in Figure 23-16 are aligned the same way, but are not monodisperse. In other cases, the fibers are aligned perpendicular or both perpendicular and parallel to the magnetic field (e.g., Fig. 23-17), the latter resulting in two planes of scattering. A synthetic fluoroamphibole was observed to align at $\pm 65^{\circ}$ to the magnetic field direction. The degree and direction of alignment has not been adequately explained; however, it appears to be more a function of the mineralogical source of the material

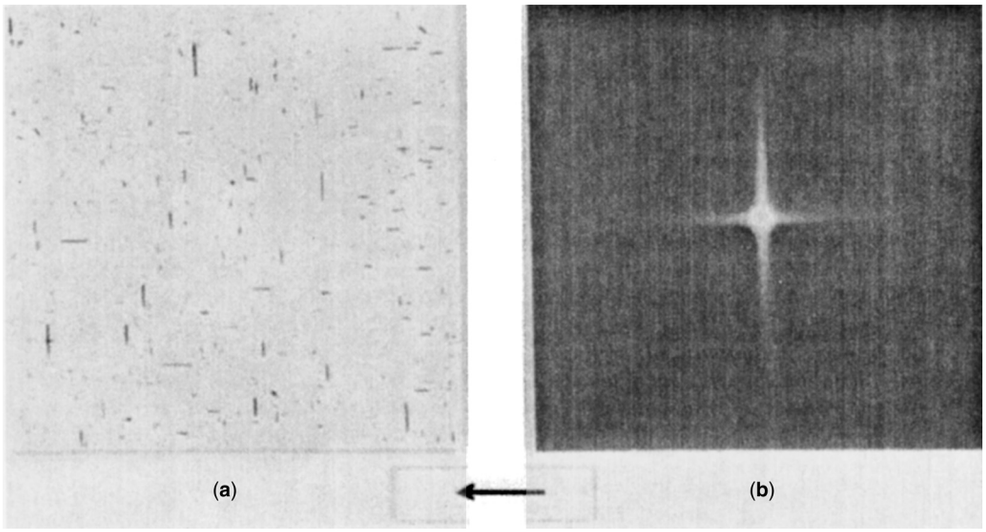

Figure 23-17 **(a)** PCM image of magnetically-aligned UICC amosite fibers suspended in celloidin on a glass slide. **(b)** Light-scattering pattern from the same fibers in aqueous suspension. The direction of the magnetic field is indicated by the arrow. Reprinted from Timbrell (1973) with permission.

rather than of the primary crystal structure. Thus, Ugandan tremolite was observed to align perpendicular to the magnetic field, while Zululand tremolite aligned parallel to the field (Timbrell 1973).

23.4.3.8 Light Scattering With a flashlight beam shining on a glass rod such that the light beam was perpendicular to the rod axis, one would expect the refracted and scattered light to be dispersed into a plane perpendicular to the rod's axis. Light scattered and refracted from microscopic fibers produces a similarly unique pattern. Such scattering patterns from magnetically aligned fibers in an aqueous suspension are given in Figures 23-15, 23-16, and 23-17. If the fiber is not perpendicular to the light beam, the light-scattering pattern is not as conveniently constrained to a plane, becoming a cone of light. The details of light scattering from infinitely long cylinders, ellipsoids, and several other regular elongated shapes can be described with Mie theory (Van de Hulst 1957; Kerker 1969). As with scattering from spherical and compact particles, the scattering from fibers with diameters larger than the light wavelength is concentrated in the forward direction. The scattering from smaller diameter fibers is less in magnitude, but more uniform in all directions around the fiber axis. In addition, the scattered light tends to be polarized in the direction parallel to the fiber axis.

The unique, planar scattering pattern for right-angle illumination has been the basis of several useful fiber detection techniques. As noted above, the fiber must be held perpendicular to the light beam axis to obtain the characteristic fiber pattern. A fiber collected on a surface such as a glass slide will generally be parallel to the slide surface, thus allowing a beam perpendicular to the slide surface to produce the narrow, planar scattering pattern from a single fiber. To obtain a characteristic scattering pattern from a group of fibers, they must be aligned using some force, such as magnetic, electric, or shear force.

Figures 23-15, 23-16, and 23-17 show the scattering patterns for several types of fibers. Note the well-defined scattering pattern for monodisperse carbon fibers (Fig. 23-15) while the broad distribution of diameters for the other fiber types produces a more diffuse pattern.

23.4.4 Laboratory Fiber Generation

Fibers are more difficult to aerosolize than compact particles because of their tendency to intertwine when in contact with one another. This tendency is the basis for some commercial properties of fibers, for example, the formation of rope and felt. Various types of fiber aerosols can be generated in various concentration ranges for instrument calibration, analytical method validation and quality assurance, and toxicology studies. Various generation mechanisms have been used to produce well-dispersed fibers.

Sample preparation of fibers for generation is an important step in producing useful aerosols. Some fibers may be available in sufficiently comminuted form for generation. Others needed to be ground, chopped, or otherwise reduced in size. Blenders and grinders have been used. Air or water suspensions can be elutriated to reduce primarily the diameter range of the fibers. One technique for glass fibers used compression to produce fiber lengths with a mode in the 5- to 20-μm range, reducing the relative number of short fragments typically produced during grinding (Hantonet al. 1998).

Nebulization of liquid suspensions has been used for generating relatively short fibers at low concentrations. Fibers larger than the nebulized droplet diameter may not be generated efficiently and if the concentration is too high, more than one fiber may be present in a droplet, resulting in fiber agglomerates.

Several researchers have used high-speed chopping of a packed fiber plug. Timbrell developed a version of this approach using a household coffee grinder (Timbrell et al. 1968). A specially ground reference material, Union Internationale Contre le Cancer (UICC) asbestos (Timbrell et al. 1968) was packed uniformly in a syringe body and pushed slowly into the rotating blades of the grinder. The consumption rate of asbestos was 0.6–1.0 g/h, though not all this was generated as an aerosol. The dispersion appeared to be largely single fibers with relatively few clumps or flocculates, though no size distribution was reported. A generator with similar operating principle and dimensions was constructed using more durable materials, including tungsten carbide blades and a stainless steel body (Fairchild et al. 1976). This device was used for both chrysotile and fibrous glass. Although there were relatively few clumps of chrysotile by number, the mass in these clumps accounted for the largest fraction of the mass distribution. Airborne concentrations of 6–8 mg/m^3 were achieved, though the feed rate could be lowered to one-fourth or increased to ten times the value used for this measurement. Fibrous glass aerosols were more successfully generated with this device (Fairchild et al. 1978).

Fluidized bed generators have also been used for creating fibrous aerosols. Fluidized beds usually consist of two phases: a powder phase, containing one or more components, and an air phase passing through the powder. The powder is "fluidized" by passing a sufficiently high airflow through it or by applying vibrational or acoustic energy. The fluidized bed may consist solely of the powder to be aerosolized or, in addition, it may also contain larger beads, microspheres, or particles that are too large to be carried away by the airflow. The larger microspheres or particles help separate the powder particles from each other and break apart the agglomerates.

A two-component fluidized bed was used for inhalation exposure experiments with fibrous glass (Carpenter et al. 1981) and crocidolite (Griffis et al. 1983). The bed consisted of a stainless steel powder mixed with the fibers as slurry and

then dried. Air passing through fluidized the bed and released the fibers, initially at a high rate, then decreasing exponentially. A similar air-fluidized bed with bronze particles as the fluidizing powder was used for generating multiple filter samples of chrysotile for a quality assurance program (Baron and Deye 1987).

Charge must be reduced on generated aerosols to produce uniform air concentrations and consistent measurements. This can be accomplished using bipolar chargers (see Chapter 15) or by modifying the generation conditions. It was found that fluidized beds produced highly charged fibers when operated with dry air. The charge level dropped about tenfold when the relative humidity of the air was increased to about 15% (Baron and Deye 1990).

A two-component fluidized bed generator with a screw feed system to continually refresh the bed with premixed powder was found to produce a constant output concentration (Tanaka and Akiyama 1984). This generator, using glass beads as the large particle fluidizing component, was found to produce a constant 6 mg/m^3 fibrous glass (from a glass fiber filter) for one week (Tanaka and Akiyama 1987). A similar system using stainless steel beads and asbestos fibers was developed by Sussman et al. (1985).

An acoustically-fluidized bed was developed to generate cellulose, ceramic and glass fibers (Weyel et al. 1984; Frazer et al. 1986; Craig et al. 1991; Blake et al. 1997). This design allowed introduction of bulk fibrous powder into the generator with relatively little processing and produced reasonably constant output concentrations over long periods of time.

A one-component fluidized bed developed by Spurny et al. (1976) and Spurny (1980) used vibrational energy to assist bed fluidization. The output of the bed for several types of asbestos was constant with time and the fiber size was somewhat controlled by the vibration frequency and amplitude. A fluidized bed generator of this type using mechanical vibration is commercially available (***PAL***).

23.4.5 Fiber Health Effects

While asbestos fibers have many useful commercial properties, there has been much concern regarding their ability to cause disease. There are three primary diseases that have been attributed to asbestos fiber exposure: asbestosis (a fibrosis or scarring of the lung tissue), mesothelioma (a cancer of the pleura or peritoneum), and lung cancer. Asbestos exposure has also been linked to gastrointestinal cancer in workers (Morgan et al. 1985), which then led to a concern over the health risks of asbestos in drinking water. However, the case for serious health risks was not generally accepted (Edelman 1988) and the U.S. Environmental Protection Agency (USEPA) set a drinking water goal of 7 million asbestos fibers >10-μm long per liter based on increased risk of developing benign intestinal polyps (USEPA 2003). Some more recent studies (Reid et al. 2004; Browne et al. 2005) have confirmed the likely absence of gastrointestinal cancer risk while others have not (Kjaerheim et al. 2005). In spite of an abundance of research into disease mechanisms of asbestos fibers, the etiologies of these diseases are still not well understood. Fiber shape appears to play a major role, although other properties, such as fiber chemistry and solubility in body fluids, clearly are also important. See Chapter 38 for further discussion on the pulmonary response to inhaled fibrous particles; that chapter also discusses health effects of some emerging fibrous particles such as carbon nanotubes.

Fiber diameter must play a role in disease, since the aerodynamic properties resulting in respiratory system deposition are strongly dependent on diameter (Timbrell 1982). In general, mineral fibers must be thinner than about 2- to 3-μm diameter to reach the thoracic region and thinner still to reach the air exchange regions of the respiratory system (Stöber et al. 1970). It has been hypothesized that short fibers have much less disease potential because macrophages in the lung can engulf these particles and remove them from the lung with relative ease. Longer fibers cannot be completely engulfed by these cells and therefore tend to remain in the lung much longer (Holt 1987). Timbrell (1982) found that clearance occurred for fibers up to 17-μm long, approximately equal to the human macrophage diameter. Use of the dielectrophoretic fiber length classifier to produce small quantities of length-classified fibers in combination with macrophage assays has confirmed that macrophages are damaged and killed by fibers slightly longer than the macrophage diameter. During macrophage death, an "oxidative burst" occurs and the macrophage produces a series of factors that are linked to lung inflammation and ultimately fibrosis (Blake et al. 1997; Ye et al. 1999). The concept of fiber dimensions as the main determinant of toxicity is often referred to as the "Stanton Hypothesis" (Stanton et al. 1981). However, it should be noted that asbestos exposure causes several diseases, and the risk for each may involve different parameters, including those not necessarily related to physical dimensions. (Dodson et al. 2003). For any airborne asbestos, fibers less than 5 μm long generally dominate the distribution, while fibers greater than 10 μm long are relatively rare (Harper et al. 2008; Dement et al. 2008). Two recent re-evaluations of fiber length in relation to mortality in asbestos mills in South Carolina (Stayner et al. 2008) and North Carolina (Loomis et al. 2010) compared exposure estimates by TEM and PCM. While TEM-based cumulative exposure estimates were found to provide stronger predictions of asbestosis and lung cancer mortality at the South Carolina mill, PCM data were a better fit for the model for lung cancer at the North Carolina mill. At the South Carolina mill, cumulative exposures based on individual fiber-size-specific categories were all found to be highly statistically significant predictors of lung cancer and asbestosis. Both lung cancer

and asbestosis were most strongly associated with exposure to thin fibers (<0.25 μm). Longer (>10 μm) fibers were found to be the strongest predictors of lung cancer, but an inconsistent pattern with fiber length was observed for asbestosis. Cumulative exposures were highly correlated across all fiber size categories in this cohort, which complicates the interpretation of the study findings. At the North Carolina mills, where fiber exposures were generally much higher than at the South Carolina mill, indicators of fiber length and diameter were also positively and significantly associated with risk of lung cancer, with exposure to longer and thinner fibers tending to be most closely associated with risk. In this study too, strong correlations among fiber-size metrics prevented modeling multiple fiber indicators simultaneously to search for evidence that specific fiber-size ranges have independent effects.

Besides shape, the chemical properties of fibers also appear to play a role. Some fibers, especially glass, have been found to dissolve in lung tissue over an extended period, reducing their potential for disease (Johnson et al. 1984; Law et al. 1990), while chrysotile fibers longer than 5 μm were found to increase in number in lung tissue, apparently due to longitudinal splitting of the fibers (Bellmann et al. 1986). *In vitro* studies have suggested that surface properties of fibers also can affect cell toxicity (Light and Wei 1977).

Extrapolation of these properties indicates that long (especially those >17 μm long), thin (<3 μm diameter) insoluble fibers may have significant disease potential, for example, several researchers have postulated more specific size ranges as causing the various diseases (Pott 1978; Lippmann 1988; Timbrell 1989).

23.4.6 Fiber Regulations

The potentially severe health effects of asbestos fiber exposure have prompted several regulatory and health research organizations to publish regulations and guidelines for controlling airborne concentrations of asbestos fibers. Since the health-based data indicates that disease at current exposure concentrations is primarily related to fiber number, most regulatory air concentration measurements are based on asbestos fiber number concentration rather than on mass concentration. In the United States for example, the Occupational Safety and Health Administration (OSHA) provides regulations for exposure to hazardous agents in industrial and other workplace settings. The OSHA regulations require that workers are not to be exposed to more than 1×10^5 fibers/m^3 [0.1 asbestos fibers/cm^3] averaged over an 8 hour period or more than 1×10^6 fibers/m^3 [1.0 fiber/cc] over 30 minutes as measured using the filter collection/phase contrast microscope (PCM) method (OSHA 1986). The Mine Safety and Health Administration (MSHA) regulates exposures in mines and mills and limits miner exposure to 1×10^5 fibers/m^3 [0.1 fibers/cm^3] for an 8-h average and 1×10^6 fibers/m^3 [1 fibers/cm^3] for a 30-min period (MSHA 2008).

The USEPA regulates environmental levels of pollutants. Apart from prohibiting visible emissions, the USEPA has not implemented limits for environmental concentrations of asbestos. However, to protect children from being exposed to asbestos in schools, the USEPA has mandated procedures for removing and measuring asbestos in schools (USEPA 1987). The USEPA has defined asbestos-containing material (ACM) as material containing more than 1% asbestos, to be measured using polarized light microscopy. After removal of ACM in schools, the USEPA requires that the airborne asbestos concentration in the cleaned area be no greater than that outside the area. Measurement is conducted using five air samples inside the area and five outside for the comparison. Analysis by transmission electron microscope (TEM) is required for monitoring the completion of all asbestos removal operations, except that the PCM can be used when removing small amounts of asbestos. Guidance documents describing methods for controlling asbestos in buildings (USEPA 1985, 1990) and for measurement of asbestos after removal (USEPA 1985) have been provided.

Because ceramic fibers have become an important commercial material, the USEPA promulgated regulations on fiber exposure as negotiated with ceramic fiber industry to keep exposure below 1.0×10^6 fibers/m^3 [1.0 fibers/cm^3].

The Consumer Product Safety Commission (CPSC) provides guidance to manufacturers regarding the material content and potential hazards of commercial products. One such product to be targeted was hairdryers, prompting measurements of their emissions (Geraci et al. 1979). Individual state agencies set regulations that are often more stringent than those of the national agencies (Abbott 1990).

NIOSH recommended elimination of exposure to airborne asbestos fibers or reduction to the lowest possible exposure levels of asbestos fiber and recommended an exposure guideline of 0.1 fiber/cm^3 based on practical limitations of PCM measurements (NIOSH 1990).

Regulation of other fibers, for example, fibrous glass and mineral wool, has generally dealt with these materials as nuisance dust. However, this may change since fibers other than asbestos have been demonstrated to have health effects in humans and animals. For instance, erionite (a fibrous zeolite) has been associated with human mesotheliomas (Baris 1980) and several man-made fibers have produced disease in animal exposure studies (Pott et al. 1987; Smith et al. 1987). Refractory ceramic fibers have produced mesothelioma in animals and nylon fibers have produced acute inflammatory reactions in the lungs of rats (Porter et al. 1999) and humans (Jones et al. 1998).

23.4.7 Measurement Techniques

There are two main classes of measurement techniques for fibers: microscopic observation of individual fibers and

light-scattering-based instruments. Other instruments described in this book also can detect fiber aerosols, but, since they are not specific for fibers, will not be considered here.

23.4.7.1 Microscopy Techniques Microscopy techniques require the collection of samples, most often on filter substrates, that are returned to the laboratory for preparation and analysis by a microscopist. Sample collection is most often carried out using a 25-mm-diameter conductive plastic cassette with a 50-mm-long inlet (cowl) to prevent direct deposition or contamination of the filter surface. The sampler provides some measure of size selection of collected fibers that varies with sampling rate and environmental conditions (Chen and Baron 1996). Fiber sampling with a classifying inlet has been proposed to remove fibers and other particles not likely to deposit in the lungs (Baron 1996). Candidate size-selective samplers have been evaluated in the laboratory and in the field (Maynard 2002; Jones et al. 2005; Lee et al. 2008). Since the aerodynamic behavior of fibers is strongly dependent on their diameter, an alternative strategy, simply to ignore fibers greater than 3-μm wide, with similar effect is used in some counting rules (World Health Organization 1997).

Four principal types of microscopes are used for fiber detection and analysis: the phase contrast light microscope (PCM), the polarized light microscope (PLM), the scanning electron microscope (SEM), and the transmission electron microscope (TEM). A review of microscope techniques for workplace and environmental asbestos measurements is given by Chatfield (1986). Descriptions of various light and electron microscopic techniques as well as pictures of many different types of fibers and particles are given in the seven-volume *Particle Atlas* (McCrone and Delly 1973). Other techniques described in Chapter 10 have also been used to analyze fibers.

Sample analysis can take place at various levels of complexity, for example, counting fibers having dimensions within prescribed size limits; determining the fiber size distribution; and measurement of the complete size distribution as well as qualitative analysis of individual fibers. The first is usually applied to establish compliance with regulations and may require some qualitative analysis as well as simple counting of fibers. The latter types of analysis are usually reserved for research studies or environmental assessments where fiber sources are unknown.

Sample preparation is extremely important for microscopic analysis, since the view of the fibers and other particles is largely two-dimensional and only a small fraction of the sample is actually observed. Thus, the particles must be uniformly distributed at optimum concentration or loading over the sample surface. If the loading is too high, fibers and particles will overlap and be difficult to analyze; if the loading is too low, it will take too long to find a useful number of fibers (Peck et al. 1986; IARC 1988). Low filter loading may also cause an overestimate of fiber concentration in some cases because fibers stand out more readily in a clean background (Cherrie et al. 1986).

23.4.7.1.1 Phase Contrast Microscopy Phase contrast microscopy (PCM) is perhaps the most often used technique for monitoring airborne concentrations of asbestos and other fibers in workplace and other environments because it can be accomplished relatively quickly and inexpensively. Primarily used for fiber number counting, PCM is an interferometric technique that enables particles with low contrast to be viewed. Light that is transmitted through the object is phase shifted relative to that transmitted through the substrate only. The phase shift is not detectable by the eye, but intensity differences are detected. The PCM transforms the phase difference to an intensity difference by forming an interference pattern using the phase-shifted and unshifted light. The limit of resolution is a function of the microscope optics, the wavelength of light, and the difference in refractive index between the object and the surrounding medium. Cellulose-based filters are used to collect the fibers and then the filter is chemically cleared on a glass slide. The fibers are observed in a phase contrast microscope at approximately 450× magnification and counted within observation fields defined by a graticule such as indicated in Figure 23-18. Between 20–100 of such fields are normally counted to obtain a statistically meaningful number of fibers (NIOSH 1994a).

The accuracy of fiber-counting techniques is not as good as that of instrumental analytical methods. For instance, most analytical methods in the *NIOSH Manual of Analytical Methods* state an overall uncertainty (combined variability and bias) of better than 10% (NIOSH 1984).

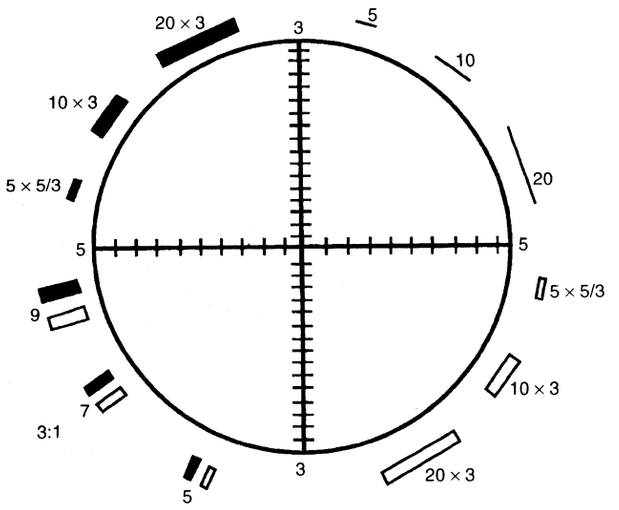

Figure 23-18 Graticule used to define counting field in a phase contrast microscope. The defined objects outside the circle are used to help determine aspect ratios and sizes of fibers that should be counted.

Under optimum analysis conditions (uniform sample deposit, no background dust interference, and optimum loading) a relative standard deviation of 0.10 (or 10%) is expected for fiber counting. Thus, the accuracy (including bias and variability) can be no better than this level. Other sources of variability and bias can occur, such as small sample size or microscopist bias. The greatest source of variability and bias is in the failure of microscopists to see very fine fibers, for example, of chrysotile asbestos. Some microscopists have been found to miss nearly all of the chrysotile fibers observed by others (Pang 2007; Pang and Harper 2008; Harper et al. 2009).

The USEPA has evaluated asbestos sample preparation techniques (USEPA 1989). Most analyses of fibrous aerosol samples are performed on filter samples that are prepared without disturbing the location of the fibers on the filter surface (direct transfer sample preparation). This approach has been taken because asbestos fibers can break up when resuspended in a liquid (especially when ultrasonicated), increasing the fiber number. When sampling other fiber types that do not break apart or when sampling problems dictate dilution of the collected sample, a liquid suspension and redeposition of the fibers may be performed (indirect transfer sample preparation). Indirect sample preparation has the advantage of allowing removal of some interfering particles as well as providing a more uniformly deposited sample.

23.4.7.1.2 Polarized Light Microscopy Polarized light microscopy (PLM) is often used to identify particles and their precursor materials to find potential sources of aerosols such as airborne fibers (OSHA 1992). It is also used to determine whether a material needs to be characterized as containing asbestos.

Light is electromagnetic energy characterized by a travel direction, an electric vibration direction, and a magnetic vibration direction that are all mutually perpendicular. Light for which the electric vibration vectors are all pointing in the same direction is plane polarized. A linear polarizing element or polarizer allows only light with the electric vibration direction in a specific direction to pass through, excluding all other light. This is the polarizing or preferred direction. Light interacts with material primarily in the direction of the electric vibration. When light travels through a material, it interacts with it and as a result, travels at some speed v which is less than it would in a vacuum where its constant speed is noted as c. The ratio of the two speeds is called the "index of refraction" or "n" and is expressed as

$$n = \frac{c}{v} \qquad \text{(Eq. 23-62)}$$

The actual speed that light travels through a material is a function of the wavelength of the light. This is known as dispersion. Some wavelengths will travel more slowly than others depending upon how strongly the light interacts with the material. As a convention, n is usually specified for the wavelength of 589 nm, which is the wavelength of the sodium D emission line. Most often, a white light source is used to illuminate particles in PLM. White light is composed of all wavelengths of visible light. One consequence of dispersion is that different wavelengths are refracted differently and thus split, as by a prism.

A technique known as "dispersion staining" uses the wavelength-dependent dispersion property to determine the indices of refraction of transparent particles. When a particle is placed in immersion oil having an index of refraction close to that of the particle, and the sample is illuminated with white light, the particle will appear colored due to the dispersion of the light as it passes through the particle and the immersion oil. The color is called a dispersion color and is used to determine the index of refraction of the particle by comparison with the color seen for glass particles of known index of refraction mounted in the same immersion oil.

Alternatively, some analysts prefer to use a traditional index-matching technique, which involves immersing particles in a succession of mounting oils or temperature varied oils to determine index of refraction (Kerr 1959). The index of refraction of the oil in which the least contrast is seen is the index of refraction of the particle. This technique is popular among mineralogists, but not among aerosol analysts. Either technique when properly carried out is very accurate.

Particles may be either isotropic or anisotropic. Isotropic materials are usually amorphous, but may be crystalline. Light traveling in any direction through the material will behave in the same manner regardless of direction. Examples of isotropic particles are unstressed fibrous glass or ceramic fibers. Anisotropic materials may be crystalline or otherwise present a differential directionality to light traveling through them. Anisotropic materials have two or three special directions through which light travels differently, each having a distinct index of refraction. These indices are associated with preferred directions in the particle. Polarized light provides a directional tool to investigate each of those special directions separately. A single polarizing element in the microscope allows the light to be aligned with the principal directions of the particle and the index of refraction can be determined independently for each direction.

In anisotropic particles, the numeric difference between the highest index of refraction n_γ (slow direction) and the lowest index of refraction n_α (fast direction) is called the birefringence. The retardation between light traveling in the slow direction and the fast direction is given as

$$\beta^r = t_p(n_\gamma - n_\alpha) \qquad \text{(Eq. 23-63)}$$

where β^r is the retardation, t_p is thickness of the particle, n_γ is high index of refraction, and n_α is low index of refraction.

In a polarizing microscope the retardation is observed as a color that results from destructive and constructive interference between white light traveling in different paths through the particle. In an anisotropic particle, part of the light travels along the slow direction and part travels along the fast direction. When the light is recombined after traveling through the particle, some of the wavelengths are diminished and some are enhanced, resulting in the particle appearing colored. This is a very rapid way of differentiating between isotropic and anisotropic particles because the isotropic particles will not exhibit color different from the background, while anisotropic ones will. Quantitative information about the particle can be obtained by measuring the thickness of the particle t and referring to a Michel-Levi chart, which is a combination color nomograph from which the numeric birefringence can be determined and then compared with compiled tables for a variety of materials.

The angle of extinction of an anisotropic particle is the maximum angular deviation between a distinct crystal growth direction and a polarization direction at which the particle exhibits minimum brightness under the condition of crossed polars. Minerals have characteristic angles of extinction, and so this value can be measured and compared with tables compiled for the purpose. In addition, certain wavelengths of light may be preferentially absorbed by a particle, giving it a distinctive color when observed in bright-field. This property can be used as part of the identification of that material. When the color is different in different directions, the particle is said to exhibit pleochroism. Identification of fibers by their specific features under polarized light is only possible for fibers greater than 1 μm in width. The finest fibers are usually identified by inference from the presence of larger, identifiable fiber bundles. Other techniques may be required to provide additional information in order to correctly identify asbestos.

X-ray diffraction (Abell 1984) and other bulk analysis techniques have also been used for asbestos and other fibers; however, these techniques are not specific for fibers and often are not sufficiently sensitive for aerosol sample analysis. Chapter 9 provides details of analytical techniques that may also be applied to asbestos or other fibers.

23.4.7.1.3 Automated Image Analysis There have been several attempts to improve the accuracy and speed and to reduce the subjectivity of microscope analysis by using automated image analysis of asbestos fiber samples (Whisnant 1975). Automated image analysis involves taking the image from a microscope, digitizing the image, and using a computer to evaluate the number and size of objects present in the image. For fiber analysis, this may involve counting the number of fibers present or obtaining a size distribution of the fibers.

An image analysis system coupled with PCM analysis of asbestos fibers was developed. The Manchester Asbestos Program (MAP) was developed at the Manchester University (U.K.) with support from the Health and Safety Executive (Kenny 1984, 1988). The MAP operated in a semi-automated mode, with the analyst selecting fields and focusing the microscope. The MAP was used for a time in various quality assurance programs but did not exhibit sufficient equivalency to human counting for continued use (Whisnant 1975).

Many image analysis systems are available with simple software for counting larger, well-defined fibers. For instance, they work reasonably well for fibrous glass insulation or synthetic organic textile fibers. Such programs typically have difficulty with asbestos fiber images because of the difficulty of detecting fibers of various diameters and curvatures, some barely visible, some overlapping, in the presence of a noisy image background containing particles of different shapes and sizes. However, with increased computer power and improved image analysis techniques, more accurate automated fiber counting may be possible in the future. A recently developed asbestos fiber counting program shows promise (Inoue et al. 1998).

Although not a complete image analysis system, one used by Lundgren and co-workers incorporated a computer display of a PCM microscope image to aid the analyst by recording the fiber count and location of each fiber during the analysis (Lundgren et al. 1995). A similar computer-based display system was coupled to a polarizing light microscope and used for quantitative measurement of tremolite fibers in dolomite (Lundgren et al. 1996).

23.4.7.2 Direct-Reading Fiber Measurement An optical particle counter has been used for detection of chrysotile fibers in a textile plant where asbestos was the primary aerosol contaminant (Rickards 1978). Other direct-reading monitors also may be used in situations where the fibers are the major constituent in the aerosol, as in laboratory studies.

A fibrous aerosol monitor was developed for more specific measurement of asbestos fibers in the presence of compact particles (Lilienfeld et al. 1979). This instrument detects fibers via a combined electrostatic alignment/optical scattering technique. A commercial version of the Fibrous Aerosol Monitor (FAM-1, ***MIE***) was produced and has undergone continuous improvement, primarily in ruggedness for field use, over the past 10 years. A more recent version with a data logger and computer control was produced (FM-7400, ***MIE***). Fiber length measurement using light scattering in the FAM was investigated (Cluff and Patitsas 1992) and indicated good correlation between lengths measured using the FAM and by SEM analysis. A dielectrophoresis-based fiber length classifier was combined with an aerodynamic sizing instrument to obtain a fiber length and diameter distribution in near real time (Baron et al. 2000).

Other direct-reading instruments combining fiber alignment and light scattering have been developed for asbestos

monitoring. Rood et al. developed a technique using fiber alignment by shear forces in an inlet tube, deposition by electrostatic precipitation and detection by differential light scattering (Rood et al. 1992). Another device, the Fibrecheck™ (***CAS***), measures scattering at multiple angles to differentiate between fibers and compact particles. No field trials of these instruments have been published. All of these devices suffer from similar problems in accurately relating observed fiber counts to the standard approach, that is, the filter collection/PCM counting method.

A general-purpose light-scattering instrument was developed that uses photomultipliers to detect light scattering in the forward direction and at three azimuthal angles, each gathering light between 27° and 140° from the forward direction. The four scattering values for each particle allowed classification of particles into shape-related groups (Kaye et al. 1996). A commercial version of this instrument is available (***BIR***). Further development of this concept used a detector array to give more complete scattering patterns (Kaye et al. 1992). An extension of the multi-angle fiber measurement approach was developed by Sachweh and co-workers (Sachweh et al. 1999). See Chapter 13 for further information about light-scattering instruments.

23.5 LIST OF SYMBOLS

a	monomer (primary particle) radius
A_c, A_p	projected areas of the aggregate and the primary particle (monomer) (Eq. 23-31)
B_r	rotational mobility
B	fiber's mechanical mobility (dyne-cm/s)
c	speed of light in vacuum
C	constant of proportionality (Eq. 23-39)
$C(d_a)$	slip correction factor for diameters d_a
$C(d_v)$	slip correction factor for the volume equivalent diameter
C_f	fiber slip correction factor
D_f	fractal dimension
d_v	volume equivalent diameter
d_p	physical size
d_m	mass equivalent diameter
d_e	envelope equivalent diameter
d_B	electric mobility diameter of the particle
d_{adj}	adjusted sphere diameter
d_a	aerodynamic diameter
d_f	diameter of the fiber
D	diffusion coefficient of particle
D_p	perimeter fractal dimension
D_r	rotational diffusion coefficient for fibers
D_{fib}	diffusion coefficient for fibers
F_D	drag force on a nonspherical particle
F_{Dve}	drag force on that particle's volume equivalent sphere
f	friction coefficient, inverse of mechanical mobility B
f°	drag per unit velocity of the fiber in the continuum regime
G	total binary dark or gray area
G_{tot}	total gray level
$g(r)$	conditional probability relating on average the density at two points separated by a distance r
$h(x)$	cutoff function for the power law
k	Boltzmann constant
k_a, α	constants near unity (Eq. 23-31)
Kn	Knudsen number
k_o	constant of order unity
l	length of the fiber
$N(L)$	number of square meshes of size L
N_{pix}	total number of dark pixel points in the picture (Eq. 23-42)
N	number of primary particles in an aggregate
N_c	cross-over N, at which constancy of N with R changes
n	index of refraction
n_γ	highest index of refraction (slow direction)
n_α	lowest index of refraction (fast direction)
q	scattering wave vector
r_{cm}	cluster center of mass
$\vec{r}_i$	position vector of the ith dark pixel (Eq. 23-42)
R	radius or a radius of gyration of an aggregate
R_g	radius of gyration
$R_{g,3}$	true, three-dimensional radius of gyration of the cluster
$R_{g,proj}$	observed for the mass-preserving projected image
R_p	perimeter radius (Eq. 23-22)
$R_{g,binary}$	binary projection radius of gyration
R_{mob}	aggregate mobility radius

R_v	volume equivalent radius
Re_p	particle Reynolds number
$S(q)$	structure factor for the fractal aggregates
T	temperature
t	thickness of the particle
V	relative velocity of the particle with respect to the surrounding gas
v	speed of light in a medium
β^r	retardation between light traveling in the slow direction and the fast direction (Eq. 23-63)
β_a	fibrosity or aspect ratio, i.e., the ratio of the length to the diameter
β	ratio of mobility radius to radius of gyration
χ^m	dynamic shape factor based on d_m
χ_c	dynamic shape factor in the continuum regime
$\chi_\parallel$, $\chi_\perp$	dynamic shape factors when the particle's symmetry axis is oriented parallel and perpendicular to the flow
χ_{ran}	orientation-averaged dynamic shape factor
μ	absolute viscosity of gas
μ_i	mean of the natural logarithm of l and d_f
ρ_f	fiber density
$\rho(r)$	density
ρ_0	standard density
ρ_e	effective particle density
$\bar{\rho}$	particle density (ρ_p) normalized by the standard density (ρ_0)
$\rho(R)$	density at point R
ρ_p	particle density
ρ_e	effective density
ξ	length parameter in Eq. 23-17
σ_i^2	variance of the natural logarithm of l and d_f,
τ	correlation between ln l and ln d_f
μ_l, μd_f, σ_l, σ_{df} and τ	parameters needed to completely define a two-dimensional size distribution

23.6 REFERENCES

Abbott, S. H. (1990). State regulatory watch. *Asbestos Issues* (December):16–25.

Abell, M. T. (1984). Chrysotile asbestos method 9000. NIOSH Manual of Analytical Methods. Cincinnati, OH, National Institute for Occupational Safety and Health.

Allen, M. D., and J. K. Briant (1978). Characterization of LMFBR fuel sodium aerosols. *Health Phys.* 35(2):237–254.

Allen, M. D., and O. G. Raabe (1982). Re-evaluation of Millikan oil drop data for the motion of small particles in air. *J. Aerosol Sci.* 13:537–547.

Allen, M. D., and O. G. Raabe (1985). Slip correction measurements of spherical solid aerosol-particles in an improved Millikan apparatus. *Aerosol Sci. Technol.* 4:269–286.

Allen, M. D., O. R. Moss, and J. K. Briant (1978). Dynamic shape factors for LMFBR mixed-oxide fuel aggregates. *J. Aerosol Sci.* 10:43–48.

Allen, M. D., J. K. Briant, and O. R. Moss (1979). Comparison of the aerodynamic size distribution of chain-like aggregates measured with a cascade impactor and a spiral centrifuge. *Am. Ind. Hyg. Assoc. J.* 40:474–481.

American Society for Testing Materials (1982). Safety and health requirements relating to occupational exposure to asbestos. E 849–82. American Society for Testing Materials, West Conshohocken, PA.

Asgharian, B., and M. N. Godo (1999). Size separation of spherical particles and fibers in an aerosol centrifuge. *Aerosol Sci. Technol.* 30(4):383–400.

Asgharian, B., and C. P. Yu (1988). Deposition of inhaled fibrous particles in the human lung. *J. Aerosol Med.* 1(1):37–50.

Asgharian, B., and C. P. Yu (1989). A simplified model of interceptional deposition of fibers at airway bifurcations. *Aerosol Sci. Technol.* 11:80–88.

Asgharian, B., L. Zhang, and C. P. Fang (1997). Theoretical calculations of the collection efficiency of spherical particles and fibers in an impactor. *Aerosol Sci. Technol.* 28:277–287.

Balásházy, I., T. B. Martonen, and W. Hofmann (1990). Fiber deposition in airway bifurcations. *J. Aerosol Med.* 3:243–260.

Baris, Y. (1980). The clinical and radiological aspects of 185 cases of malignant pleural mesothelioma. In: *Biological Effects of Mineral Fibres*, J. C. Wagner (ed.). Lyon, France, International Agency for Research on Cancer, 2:937–947.

Baron, P. A. (1996). Application of the thoracic sampling definition to fiber measurement. *Am. Ind. Hyg. Assoc. J.* 57:820–824.

Baron, P. A., and G. J. Deye (1987). Generation of replicate asbestos aerosol samples for quality assurance. *Appl. Ind. Hyg.* 2:114–118.

Baron, P. A., and G. J. Deye (1990). Electrostatic effects in asbestos sampling I: Experimental measurements. *Am. Ind. Hyg. Assoc. J.* 51:51–62.

Baron, P. A., and S. A. Shulman (1987). Evaluation of the Magiscan image analyzer for asbestos fiber counting. *Am. Ind. Hyg. Assoc. J.* 48:39–46.

Baron, P. A., G. J. Deye, and J. Fernback (1994). Length separation of fibers. *Aerosol Sci. Technol.* 21:179–192.

Baron, P. A., P. Gao, G. J. Deye, and A. C. Maynard (1998). Performance of a fiber length classifier. *J. Aerosol Sci.* 29(Suppl. 1):S11–S12.

Baron, P. A., G. J. Deye, J. E. Fernback, and W. G. Jones (2000). Direct-reading measurement of fiber length/diameter distributions.

Beard, M. E., and H. L. Rook. Advances in environmental measurement methods for asbestos. Boulder CO, American Society for Testing Materials. STP 1342.

Bellmann, B., H. König, H. Muhle, and F. Pott (1986). Chemical durability of asbestos and of man-made mineral fibres in vivo. *J. Aerosol Sci.* 17:341–345.

Blake, T., V. Castranova, D. Schwegler-Berry, G. J. Deye, P. Baron, C. Li, and W. Jones (1997). Effect of fiber length on glass microfiber cytotoxicity. *J. Tox. Environ. Health* 54A:243–259.

Brasil, A. M., T. L. Farias, and M. G. Carvalho (1999). A recipe for image characterization of fractal-like aggregates, *J. Aerosol Sci.* 30:1379–1389.

Brockmann, J. E., and D. J. Rader (1990). APS response to nonspherical particles and experimental determination of dynamic shape factor. *Aerosol Sci. Technol*. 13:162–172.

Browne M. L., D. Varadarajulu, E. L. Lewis-Michl, and E. F. Fitzgerald (2005). Cancer incidence and asbestos in drinking water, town of Woodstock, New York, 1980–1998. *Environ. Res.* 98:224–232.

Burke, W. A., and N. A. Esmen (1978). The inertial behavior of fibers. *Amer. Ind. Hyg. Assoc. J.* 39:400–405.

Cai, J., and C. M. Sorensen (1994). Diffusion of fractal aggregates in the free molecular regime. *Phys. Rev.* E50:3397–3400.

Cai, J., N. Lu, and C. M. Sorensen (1993). Comparison of size and morphology of soot aggregates as determined by light scattering and electron microscope analysis. *Langmuir* 9: 2861–2068.

Cai, J., N. Lu, and C. M. Sorensen (1995a). Analysis of fractal cluster morphology parameters: structural coefficient and density autocorrelation function cutoff. *J. Colloid Inter. Sci.* 171:470–473.

Cai, J., N. Lu, and C. M. Sorensen (1995b). Fractal cluster size distribution measurement using static light scattering. *J. Colloid Inter. Sci.* 174:456–460.

Carpenter, R. L., J. A. Pickrell, B. V. Mokler, H. C. Yeh, and P. B. DeNee (1981). Generation of respirable glass fiber aerosols using a fluidized bed aerosol generator. *Am. Ind. Hyg. Assoc. J.* 42:777–784.

Chan, P., and B. Dahneke (1981). Free-molecule drag on straight chains of uniform spheres. *J. Appl Phys.* 52:3106.

Chatfield, E. J. (1986). Asbestos measurements in workplaces and ambient atmospheres. In: *Electron Microscopy in Forensic, Occupational and Environmental Health Sciences*. S. Basu and J. R. Millette (eds.). New York, Plenum.

Chen, C.-C., and P. A. Baron (1996). Aspiration efficiency and wall deposition in the fiber sampling cassette. *Am. Ind. Hyg. Assoc. J.* 52(2):142–152.

Chen, Y. K., and C. P. Yu (1990). Sedimentation of charged fibers from a two-dimensional channel flow. *Aerosol Sci. Technol*. 12:786–792.

Chen, B. T., R. Irwin, Y. S. Cheng, M. D. Hoover, and H. C. Yeh (1993). Aerodynamic behavior of fiber-like and disk-like particles in a Millikan cell apparatus. *J. Aerosol Sci.* 24:181–195.

Cheng, M. T., G. W. Xie, M. Yang, and D. T. Shaw (1991). Experimental characterization of chain-aggregate aerosol by electrooptic scattering. *Aerosol Sci. Technol.* 14(1):74–81.

Cheng, Y.-S. (1986). Bivariate lognormal distribution for characterizing asbestos fiber aerosols. *Aerosol Sci. Technol*. 5(3): 359–368.

Cheng, Y.-S., M. D. Allen, D. P. Gallegos, and H.-C. Yeh (1988a). Drag force and slip correction of aggregate aerosols. *Aerosol Sci. Technol*. 8:199–214.

Cheng, Y.-S., H.-C. Yeh, and M. D. Allen (1988b). Dynamic shape factor of a plate-like particle. *Aerosol Sci. Technol.* 8:109–124.

Cherrie, J., A. D. Jones, and A. M. Johnston (1986). The influence of fiber density on the assessment of fiber concentration using the membrane filter method. *Am. Ind. Hyg. Assoc. J.* 47:465–474.

Chissick, S. S., and R. Derricott (1983). *Asbestos: Properties, Applications and Hazards*. Chichester, John Wiley & Sons.

Cho, K., C. J. Hogan, and P. Biswas (2007). Study of the mobility, surface area and sintering behavior of agglomerates in the transition regime by tandem differential mobility analysis. *J. Nanopart. Res.* 9:1003–1012.

Clift, R., J. R. Grace, and M. E. Weber (1978). *Bubbles, Drops and Particles*. New York, Academic.

Cluff, D. L., and A. J. Patitsas (1992). Size characterization of asbestos fibers by means of electrostatic alignment and light-scattering techniques. *Aerosol Sci. Technol*. 17(3):186–198.

Cox, R. G. (1970). The motion of long slender bodies in a viscous fluid I: General theory. *J. Fluid Mech*. 44:791.

Craig, D. K., C. A. Lapin, and G. E. Butterfield (1991). The generation and characterization of silicon carbide whiskers (fibers) for inhalation toxicology studies. *Am. Ind. Hyg. Assoc. J.* 52(8):315–319.

Dahneke, B. E. (1973a). Slip correction factors for nonspherical bodies—I Introduction and continuum flow. *J. Aerosol Sci.* 4:139–145.

Dahneke, B. E. (1973b). Slip correction factors for nonspherical bodies—II Free molecule flow. *J. Aerosol Sci.* 4:147–161.

Dahneke, B. E. (1973c). Slip correction factors for nonspherical bodies—III The form of the general law. *J. Aerosol Sci.* 4:163–170.

Dahneke, B. (1982). Viscous resistance of straight-chain aggregates of uniform spheres. *Aerosol Sci. Technol*. 1:179–185.

de la Mora, J. F., L. de Juan, T. Eichler, and J. Rosell (1998). Differential mobility analysis of molecular ions and nanometer particles. *Trac-Trends in Analyt. Chem.* 17:328–339.

de la Mora, J. F., L. de Juan, K. Liedtke, and A. Schmidt-Ott (2003). Mass and size determination of nanometer particles by means of mobility analysis and focused impaction. *J. Aerosol Sci.* 34:79–98.

DeCarlo, P. F., J. G. Slowik, D. R. Worsnop, P. Davidovits, and J. L. Jimenez (2004). Particle morphology and density characterization by combined mobility and aerodynamic diameter measurements. Part 1: Theory. *Aerosol Sci. Technol.* 38:1185–1205.

Dement, J. M. (1990). Overview: Workshop on fiber toxicology research needs. *Environ. Health Perspec*. 88:261–268.

Dement, J. M., and K. M. Wallingford (1990). Comparison of phase contrast and electron microscopic methods for evaluation of occupational asbestos exposures. *Appl. Occup. Environ. Hyg*. 5:242–247.

Dement, J. M., E. D. Kuempel, R. D. Zumwalde, R. J. Smith, L. T. Stayner, and D. Loomis (2008). Development of a fibre size-specific job-exposure matrix for airborne asbestos fibres. *Occup. Environ. Med.* 65:605–612.

Dhaubhadel, R., A. Pierce, A. Chakrabarti, and C. M. Sorensen (2006). Hybrid superaggregate morphology as a result of aggregation in a cluster-dense aerosol. *Phys. Rev. E*. 73:011404.

Dobbins, R. A. and C. M. Magaridis (1987). Morphology of flame-generated soot as determined by thermophoretic sampling. *Langmuir* 3:254–259.

Dodson, R. F., M. A. L. Atkinson, and J. L. Levin (2003). Asbestos fiber length as related to potential pathogenicity: a critical review. *Am. J. Ind. Med.* 44:291–297.

Edelman, D. A. (1988). Exposure to asbestos and the risk of gastrointestinal cancer: a reassessment. *Br. J. Ind. Med.* 45:75–82.

Fairchild, C. I., L. W. Ortiz, H. J. Ettinger, and M. I. Tillery (1976). Aerosol research and development related to health hazard analysis. LA-6277-PR. Los Alamos, NM, Los Alamos Scientific Laboratory.

Fairchild, C. I., L. W. Ortiz, M. I. Tillery, and H. J. Ettinger (1978). Aerosol research and development related to health hazard analysis. LA-7380-PR. Los Alamos, NM, Los Alamos Scientific Laboratory.

Family, F. (1991). Fractals. In: *Encyclopedia of Physics*, 2 ed., R. G. Lerner and G. L. Trigg (eds.). New York, VCH, p. 414.

Family, F., and D. P. Landau (1984). Kinetics of Aggregation and Gelation. In: *Proceedings of the International Topical Conference on Kinetics of Aggregation and Gelation*, F. Family, and D. P. Landau (eds.). Elsevier Science Pub. Co. in Amsterdam, Athens, Georgia.

Forrest, S. R., and T. A. Witten Jr. (1979). Long-range correlations in smoke-particle aggregates. *J. Phys. A: Math. Gen*. 12:L109–L117.

Frazer, D. G., V. Robinson, K. Jayaraman, K. C. Weber, D. S. DeLong, and C. Glance (1986). Improved operating parameters for the Pitt 3 aerosol generator during resuspension of respirable cotton dust. *The Tenth Cotton Dust Research Conference*, National Cotton Council, Memphis, TN.

Friedlander, S. K., H. D. Jang, and K. H. Ryu (1998). Elastic behavior of nanoparticle chain aggregates. *Appl. Phys. Lett.* 72:173–175.

Fu, T.-H., M.-T. Cheng, and D. Shaw (1990). Filtration of chain aggregate aerosols by model screen filter. *Aerosol Sci. Technol*. 13(2):151–161.

Fuchs, N. A. (1964). *The Mechanics of Aerosols*. Oxford, Pergamon.

Gallily, I. (1971). On the drag experienced by a spheroidal, small particle in a gravitational and electrostatic field. *J. Colloid Interface Sci.* 36(3):325–339.

Gallily, I., and A. D. Eisner (1979). On the orderly nature of the motion of nonspherical aerosol particles I. *Deposition from a laminar flow. J. Colloid Interface Sci.* 68:320–337.

Gallily, I., D. Schiby, A. H. Cohen, W. Holländer, D. Schless, and W. Stöber (1986). On the inertial separation of nonspherical aerosol particles from laminar flows. I. The cylindrical case. *Aerosol Sci. Technol*. 5(2):267–286.

Gangopadhyay, S., I. Elminyawi, and C. M. Sorensen (1991). Optical structure factor measurements of soot particles in a premixed flame. *Appl. Optics* 30:4859–4864.

Gelbard, F. (1982). MAEROS User Manual. NUREG/CR-1391 SAND80-0822. Albuquerque, NM, Sandia National Laboratories.

Geller, M., S. Biswas, and C. Sioutas (2006). Determination of particle effective density in urban environments with a differential mobility analyzer and aerosol particle mass analyzer. *Aerosol Sci. Technol*. 40:709–723.

Gentry, J. W., K. R. Spurny, J. Schörmann, and H. Opiela (1983). Measurement of the diffusion coefficient of asbestos fibers. In: *Aerosols in the Mining and Industrial Work Environments*, V. A. Marple and B. Y. H. Liu (eds.). Ann Arbor, MI, Ann Arbor Science. 2:597–612.

Gentry, J. W., K. R. Spurny, S. A. Soulen, and J. Schörmann (1988). Measurements of the diffusion coefficients of ultrafine asbestos fibers. *J. Aerosol Sci.* 19(7):1041–1044.

Geraci, C., P. A. Baron, J. W. Carter, and D. L. Smith (1979). Testing of hair dryer emissions. IA-79-29. Cincinnati, OH, National Institute for Occupational Safety and Health.

Gieseke, J. A., L. D. Reed, H. Jordan, and K. W. Lee (1977). Characteristics of agglomerates of sodium oxide aerosols. BMI-NUREG-1977 NRC-7. Battelle Columbus Laboratories.

Gonda, I. and A. F. A. E. Khalik (1985). On the calculation of aerodynamic diameters of fibers. *Aerosol Sci. Technol.* 4:233–238.

Griffis, L. C., J. A. Pickrell, R. L. Carpenter, R. K. Wolff, S. J. McAllen, and K. L. Yerkes (1983). Deposition of crocidolite asbestos and glass microfibers inhaled by the beagle dog. *Am. Ind. Hyg. Assoc. J.* 44(3):216–222.

Griffiths, W. D., and N. P. Vaughan (1986). The aerodynamic behaviour of cylindrical and spheroidal particles when settling under gravity. *J. Aerosol Sci.* 17(1):53–65.

Griffiths, W. D., L. C. Kenny, and S. T. Chase (1985). The electrostatic separation of fibres and compact particles. *Ann. Occup. Hyg*. 16(3):229–243.

Guinier, A., G. Fournet, C. B. Walker, and K. L. Yudowitch (1955). *Small Angle Scattering of X-Rays*. New York, John Wiley and Sons.

Gwaze P., O. Schmid, H. J. Annegarn, M. O. Andreae, J. Huth, and G. Helas (2006). Comparison of three methods of fractal analysis applied to soot aggregates from wood combustion. *J. Aerosol Sci.* 37:820–838.

Hanton, D. Y., H. Furtak, and H. G. Grimm (1998). Preparation and handling conditions of MMVF for in-vivo experiments. *Aerosol Sci. Technol*. 29:449–456.

Harper, M (2008). Naturally occurring asbestos. *J. Environ. Monit.* 10:1394–1408.

Harper, M., E. G. Lee, S. S. Doorn, and O. Hammond (2008). Differentiating non-asbestiform amphibole and amphibole

asbestos by size characteristics. *J. Occup. Environ. Hyg*. 5:761–770.

Harper, M., J. E. Slaven, and T. W. S. Pang (2009). Continued participation in an asbestos fiber-counting proficiency test with relocatable grid slides. *J. Environ. Monit*. Advance web publication. DOI: 10.1039/B813893A.

Helton, J. C., R. L. Iman, J. D. Johnson, and C. D. Leigh (1986). Uncertainty and sensitivity analysis of a dry containment test problem for the MAEROS aerosol model. SAND85-2795. Albuquerque, NM, Sandia National Laboratories.

Hering, S. V., and M. R. Stolzenburg (1995). Online determination of particle-size and density in the nanometer-size range. *Aerosol Sci. Technol*. 23:155–173.

Hinds, W. C. (1999). *Aerosol Technology*. New York, John Wiley and Sons.

Holst, E., and T. Schneider (1985). Fibre size characterization and size analysis using general and bivariate log-normal distributions. *J. Aerosol Sci.* 5:407–413.

Holt, P. F. (1987). *Dust and Disease*. New York, John Wiley and Sons.

IARC (1988). Man-made mineral fibers and radon. IARC monographs of the evaluation of the carcinogenic risk of chemicals in humans. Lyon, France, International Agency for Research on Cancer. 43:33–171.

Iles, P. J. (1990). Size selection of fibres by cyclone and horizontal elutriator. *J. Aerosol Sci.* 21(6):745–760.

Inoue, Y., A. Kaga, K. Yamaguchi, and S. Kamoi (1998). Development of an automatic system for counting asbestos fibers using image processing. *Part. Sci. Technol*. 16:263–279.

Johnson, D. L., D. Leith, and P. C. Reist (1987). Drag on nonspherical orthotropic aerosol particles. *J. Aerosol Sci.* 18(1):87–97.

Johnson, N. F., D. M. Griffiths, and R. J. Hill (1984). Size distribution following long term inhalation of MMMFn: *Biological Effects of Man-Made Mineral Fibers.* Copenhagen, World Health Organization. 2:102–125.

Johnston, A. M., J. H. Vincent, and A. D. Jones (1985). Measurements of electric charge for workplace aerosols. *Ann. Occup. Hyg*. 29(2):271–284.

John, G., J. G. Kirkwood, J. Riseman (1948). The intrinsic viscosities and diffusion constants of flexible macromolecules in Solution, *J. Chem. Phys.* 16(6):565–573.

Jones, A. D., A. M. Johnston, and J. H. Vincent (1983). Static electrification of airborne asbestos dust. In: *Aerosols in the Mining and Industrial Work Environment*, V. A. Marple and B. Y. H. Liu (eds.). Ann Arbor, MI, Ann Arbor Science, 2:613–632.

Jones A. D., R. J. Aitken, J. F. Fabries, E. Kauffer, G. Lidén, A. Maynard, G. Riediger, and W. Sahle (2005). Thoracic size selective sampling of fibers: Performance of four types of thoracic sampler in laboratory tests. *Ann. Occup. Hyg*. 49:481–92.

Jones, W. G., C. Piacitelli, D. Schwegler-Berry, and J. Burkhart (1998). *Environmental Study of Nylon Flocking Process.* Cincinnati, OH, National Institute for Occupational Safety and Health.

Jullien, R., R. Thouy, and F. Ehrburger-Doll (1994). Numerical investigation of two-dimensional projections of random fractal aggregates. *Phys. Rev.* E50:3878–3882.

Karg, E. (2000). The density of ambient particles from combined DMA and APS data. *J. Aerosol Sci.* 31:759–760.

Kasper, G. (1977). On the density of sodium chloride aerosols formed by condensation. *Journal of Colloid and Interface Science*, 62:359–360.

Kasper, G. (1982). Dynamics and measurement of smokes. II. The aerodynamic diameter of chain aggregates in the transition regime. *Aerosol Sci. Technol*. 1(2):201–216.

Kasper, G. (1983). Note on the slip coefficient of doublets of spheres. *J. Aerosol Sci.* 14(6):753–754.

Kasper, G., S. N. Shon, and D. T. Shaw (1980). Controlled formation of chain aggregates from very small metal oxide particles. *Am. Ind. Hyg. Assoc. J.* 41:288–296.

Kasper, G., and D. T. Shaw (1983). Comparative size distribution measurements on chain aggregates. *Aerosol Science and Technology* 2:369–381.

Kasper, G., and H. Y. Wen (1984). Dynamics and measurement of smokes. 4. Comparative measurements with an aerosol centrifuge and an aerodynamic particle sizer aps33 using sub-micron chain aggregates. *Aerosol Sci. Technol*. 3:405–409.

Kaye, P. H., E. Hirst, J. M. Clark, and F. Micheli (1992). Airborne particle shape and size classification from spatial light scattering profiles. *J. Aerosol Sci.* 23(6):597–612.

Kaye, P. H., K. Alexander-Buckley, E. Hirst, S. Saunders, and J. M. Clark (1996). A real-time monitoring system for airborne particle shape and size analysis. *J. Geophys. Res.* 101:19215–221.

Kelly, W. P., and P. H. McMurry (1992). Measurement of particle density by inertial classification of differential mobility analyzer-generated monodisperse aerosols. *Aerosol Sci. Technol*. 17:199–212.

Kelse, J. W., and C. S. Thompson (1989). The regulatory and mineralogical definitions of asbestos and their impact on amphibole dust analysis. *Am. Ind. Hyg. Assoc. J.* 50:613–622.

Kenny, L. C. (1984). Asbestos fibre counting by image analysis—The performance of the Manchester Asbestos Program on Magiscan. *Ann. Occup. Hyg*. 28:401–415.

Kenny, L. C. (1988). Automated analysis of asbestos clearance samples. *Ann. Occup. Hyg*. 32(1):115–128.

Kerker, M. (1969). *The Scattering of Light and Other Electromagnetic Radiation.* New York, Academic.

Kerr, P. F. (1959). *Optical Mineralogy*, 3 ed. New York, McGraw-Hill.

Khlystov, A., C. Stanier, and S. N. Pandis (2004). An algorithm for combining electrical mobility and aerodynamic size distributions data when measuring ambient aerosol. *Aerosol Sci. Technol*. 38:229–238.

Kim, S. H., and M. R. Zachariah (2005). In-flight size classification of carbon nanotubes by gas phase electrophoresis. *Nanotechnology* 16:2149–2152.

Kim, S. H., G. W. Mulholland, and M. R. Zachariah (2007). Understanding ion-mobility and transport properties of aerosol nanowires. *J. Aerosol Sci.* 38:823–842.

Kirkwood, J. G. and J. Riseman (1948). The intrinsic viscosities and diffusion constants of flexible macromolecules in solution. *J. Chem. Phys.* 16:565–573.

Kjaerheim, K., B. Ulvestad, J. I. Martinsen, and A. Andersen (2005). Cancer of the gastrointestinal tract and exposure to asbestos in drinking water among lighthouse keepers (Norway). *Cancer Causes Control* 16:593–598.

Kolb, M., R. Botet, and R. Jullien (1983). Scaling of kinetically growing clusters. *Phys. Rev. Lett.* 51:1123–1126.

Kops, J., G. Dibbets, L. Hermans, and J. F. Van der Vate (1975). The aerodynamic diameter of branched-chain-like aggregates. *J. Aerosol Sci.* 6(5):329–334.

Kousaka, Y., Y. Endo, H. Ichitsuo, and M. Alonso (1996). Orientation-specific dynamic shape factors for doublets and triplets of spheres in the transition regime. *Aerosol Sci. Technol.*, 24:36–44.

Köylü, U. O., and G. M. Faeth (1992). Structure of overfire soot in buoyant turbulent diffusion flames at long residence times. *Combust. Flame* 89:140–156.

Köylü, U. O., G. M. Faeth, T. L. Farias, and M. G. Carvalho (1995). Fractal and projected structure properties of soot aggregates. *Combust. Flame* 100:621–633.

Laframboise, J. G., and J.-S. Chang (1977). Theory of charge deposition on charged aerosol particles of arbitrary shape. *J. Aerosol Sci.* 8:331–338.

Langer, A. (1974). The subject of continuous vigilance. *Environ. Health Perspect*. 9:53–56.

Langer, A. M., A. D. Mackler, and F. D. Pooley (1974). Electron microscopical investigation of asbestos fibers. *Environ. Health Perspec*. 9:63–80.

Law, B. D., W. B. Bunn, and T. W. Hesterburg (1990). Solubility of polymeric organic fibers and manmade vitreous fibers in gambles solution. *Inhal. Tox*. 2:321–339.

Lee, E. G., M. Harper, J. Nelson, P. J. Hintz, and M. E. Andrew (2008). A comparison of the CATHIA-T sampler, the GK2.69 cyclone and the standard cowled sampler for thoracic fiber concentrations at a taconite ore-processing mill. *Ann. Occup. Hyg*. 52:55–62.

Light, W. G., and E. T. Wei (1977). Surface charge and asbestos toxicity. *Science* 265:537–539.

Lilienfeld, P. (1985). Rotational electrodynamics of airborne fibers. *J. Aerosol Sci.* 16(4):315–322.

Lilienfeld, P., P. Elterman, and P. Baron (1979). Development of a prototype fibrous aerosol monitor. *Amer. Ind. Hyg. Assoc. J.* 40(4):270–282.

Lin, M. Y., H. M. Lindsay, D. A. Weitz, R. C. Ball, R. Klein, and P. Meakin (1990). Universal reaction-limited colloid aggregation. *Phys. Rev. A* 41:2005–2020.

Lipowicz, P. J., and H. C. Yeh (1989). Fiber dielectrophoresis. *Aerosol Sci. Technol*. 11:206–212.

Lippmann, M. (1988). Asbestos exposure indices. *Environ. Res.* 46:86–106.

Loomis, D., J. Dement, D. Richardson, and S. Wolf (2010). Asbestos fibre dimensions and lung cancer mortality among workers exposed to chrysotile. *Occup. Environ. Med.* 67:580–584.

Lundgren, L., S. Lundström, I. Laszlo, and B. Westling (1995). Modern fibre counting—A technique with the phase-contrast microscope on-line to a Macintosh computer. *Ann. Occup. Hyg*. 39(4):455–467.

Lundgren, L., S. Lundström, G. Sundström, G. Bergman, and S. Krantz (1996). A quantitative method using a light microscope on-line to a Macintosh computer for the analysis of tremolite fibres in dolomite. *Ann. Occup. Hyg*. 40:197–209.

Mackowski, D. W. (2006). Monte Carlo simulation of hydrodynamic drag and thermophoresis of fractal aggregates of spheres in the free-molecular flow regime. *J. Aerosol Sci.* 37:242–259.

Mandelbrot, B. B. (1977). *Fractals: Form, Chance and Dimension.* San Francisco, W. H. Freeman.

Mandelbrot, B. B. (1983). *The Fractal Geometry of Nature*. New York, W. H. Freeman.

Maricq, M. M., D. H. Podsiadlik, and R. E. Chase (2000). Size distributions of motor vehicle exhaust PM: A comparison between ELPI and SMPS measurements. *Aerosol Sci. Technol.* 33:239–260.

Martin, J. E., and B. J. Ackerson (1985). Static and dynamic light scattering from fractals. *Phys. Rev. A* 31:1180–1182.

Martonen, T. B., and D. L. Johnson (1990). Aerodynamic classification of fibers with aerosol centrifuges. *Part. Sci. Technol.* 8:37–53.

Maynard, A. (2002). Thoracic size-selection of fibres: Dependence of penetration on fibre length for five thoracic samplers. *Ann. Occup. Hyg*. 46:511–522.

McCrone, W. C., and J. G. Delly (1973). *The Particle Atlas*. Ann Arbor, MI, Ann Arbor Science.

McMurry, P. H., X. Wang, K. Park, and K. Ehara (2002). The relationship between mass and mobility for atmospheric particles: A new technique for measuring particle density. *Aerosol Sci. Technol*. 36:227–238.

Meakin, P. (1983). Formation of fractal clusters and networks by irreversible diffusion-limited aggregation. *Phys. Rev. Lett.* 51:1119–1122.

Meakin, P. (1984). Effects of cluster trajectories on cluster-cluster aggregations: A comparison of linear and Brownian trajectories in two- and three-dimensional simulations. *Phys. Rev. A* 29:997–999.

Meakin, P. (1988). Fractal aggregates. *Adv. Coll. Interface Sci.* 28:249–331.

Meakin, P., Z.-Y. Chen, and J. M. Deutch (1985). The translational friction coefficient and time dependent cluster size distribution of three dimensional cluster-cluster aggregation. *J. Chem. Phys.* 82:3786–3789.

Meakin, P., B. Donn, and G. W. Mulholland (1989). Collisions between point masses and fractal aggregates. *Langmuir* 5:510–518.

Meakin, P., C. Zhong-Ying, and J. M. Deutch (1985). Dependent cluster size distribution of three dimensional cluster-cluster aggregation. *J. Chem. Phys.* 82, 3786–3789.

Medalia, A. I. (1967). Morphology of aggregates. *J. Coll. Interface Sci.* 24:393–404.

Medalia, A. I., and F. A. Heckman (1969). Morphology of aggregates-II. Size and shape factors of carbon black aggregates from electron microscopy. *Carbon* 7:567–582.

Megaridis, C. M., and R. A. Dobbins (1990). Morphological description of flame generated materials. *Combust. Sci. Tech.* 71:95-109.

Michaels, L., and S. S. Chissick (1979). *Asbestos: Properties, Applications and Hazards.* Chichester, UK, John Wiley and Sons.

Morawska, L., G. Johnson, Z. D. Ristovski, and V. Agranovski (1999). Relation between particle mass and number for submicrometer airborne particles. *Atmos. Environ.* 33:1983–1990.

Morgan, R. W., D. E. Foliart, and O. Wong, (1985). Asbestos and gastrointestinal cancer—a review of the literature. *West. J. Med.* 143:60–65.

MSHA, Mine Safety and Health Administration (2008). Asbestos exposure limit, Final rule. 30 CFR Parts 56, 57 and 71. *Federal Register* vol. 73 No. 41, Feb 29 2008, 11284–11304.

NIOSH, National Institute for Occupational Safety and Health (1976). Revised Recommended Asbestos Standard. DHEW (NIOSH) Publication No. 77–169. Cincinnati, OH, National Institute for Occupational Safety and Health. [http://www.cdc.gov/niosh/docs/77-169/]. Date accessed: June 30, 2008.

NIOSH, National Institute for Occupational Safety and Health. (1977). Occupational Exposure to Fibrous Glass. DHEW (NIOSH) Publication No. 77–152. Cincinnati, OH, National Institute for Occupational Safety and Health.

NIOSH, National Institute for Occupational Safety and Health (1984). NIOSH testimony to the U.S. Department of Labor: Statement of the National Institute for Occupational Safety and Health. *Presented at the public hearing on occupational exposure to asbestos, June 21, 1984*. Cincinnati, OH: U.S. Department of Health and Human Services, Public Health Service, Centers for Disease Control, National Institute for Occupational Safety and Health.

NIOSH, National Institute for Occupational Safety and Health (1990). Testimony of the National Institute for Occupational Safety and Health on the Occupational Safety and Health Administration's Notice of Proposed Rulemaking on Occupational Exposure to Asbestos, Tremolite, Anthophyllite, and Actinolite. U.S. Department of Labor Docket No. H-033d, May 9, 1990.

NIOSH, National Institute for Occupational Safety and Health. (1994a). Asbestos and Other Fibers by PCM. Method 7400. In: *NIOSH Manual of Analytical Methods*, 4 ed. Cincinnati, OH, National Institute for Occupational Safety and Health.

NIOSH, National Institute for Occupational Safety and Health. (1994b). Asbestos by TEM Method 7402. In *NIOSH Manual of Analytical Methods*, 4 ed. Cincinnati, OH, National Institute for Occupational Safety and Health.

NIOSH, National Institute for Occupational Safety and Health. (2005). Comments on the Mine Safety and Health Administration Proposed Rule on Asbestos Exposure Limit, October 13, 2005. www.cdc.gov/niosh/review/public/099/pdfs/Asbestosmsha_final%202005_proposed%20rule.pdf

Oh, C., and C. M. Sorensen (1997). The effect of monomer overlap on the morphology of fractal aggregates. *J. Coll. Interface Sci.* 193:17–25.

Oh, C., and C. M. Sorensen (1998). Structure factor of diffusion-limited aggregation clusters: Local structure and non-self-similarity. *Phys. Rev. E* 57:784–790.

Oh, C., and C. M. Sorensen (1999). Scaling approach for the structure factor of a generalized system of scatterers. *J. Nanopart. Res.* 1:369–377.

OSHA, Occupational Safety and Health Administration. (1986). Occupational exposure to asbestos, tremolite, anthophyllite, and actinolite asbestos; final rules. 29 CFR Part 1910.1001 and 1926. Occupational Safety and Health Administration, Washington, DC.

OSHA, Occupational Safety and Health Administration. (1992). Polarized light microscopy of asbestos method ID-191, OSHA Manual of Analytical Methods. Occupational Safety and Health Administration. http://www.osha.gov/dts/sltc/methods/inorganic/id191/id191.html

Pang, T. W. S. (2007). A new parameter to evaluate the quality of fiber count data of slides of relocatable fields. *J. Occup. Environ. Hyg.* 4:129–144.

Pang, T. W. S., and M. Harper (2008). The quality of fiber counts using improved slides with relocatable fields. *J. Environ. Monit.* 10:89–95.

Park, K., F. Cao, D. B. Kittelson, and P. H. McMurry (2003). Relationship between particle mass and mobility for diesel exhaust particles. *Environ. Sci. Technol.* 37:577–583.

Park, K., D. B. Kittelson, M. R. Zachariah, and P. H. McMurry (2004). Measurement of inherent material density of nanoparticle agglomerates. *J. Nanopart. Res.* 6:267–272.

Park, K., D. Dutcher, M. Emery, J. Pagels, H. Sakurai, J. Scheckman, S. Qian, M. R. Stolzenburg, X. Wang, J. Yang, and P. H. McMurry (2008). Tandem measurements of aerosol properties—A review of mobility techniques with extensions. *Aerosol Sci. Technol.* 42:801–816.

Peck, A. S., J. J. Serocki, and L. C. Dicker (1986). Sample density and the quantitative capabilities of PCM analysis for the measurement of airborne asbestos. *Am. Ind. Hyg. Assoc. J.* 47:A230–A234.

Pierce, F., C. M. Sorensen, and A. Chakrabarti (2006). Computer simulation of diffusion-limited cluster-cluster aggregation with an Epstein drag force. *Phys. Rev. E* 74:021411.

Pitz, M., J. Cyrys, E. Karg, A. Wiedensohler, H. E. Wichmann, and J. Heinrich (2003). Variability of apparent particle density of an urban aerosol. *Environ. Sci. Technol.* 37:4336–4342.

Porter, D. W., V. Castranova, R. A. Robinson, A. F. Hubbs, R. R. Mercer, J. Scabilloni, T. Goldsmith, D. Schwegler-Berry, L. Battelli, R. Washko, J. Burkhart, C. Piacitelli, M. Whitmer, and W. Jones (1999). Acute inflammatory reaction in rats after intratracheal instillation of material collected from a nylon flocking plant. *J. Tox. Environ. Health. Part A* 57:25–45.

Pott, F. (1978). Some aspects on the dosimetry of the carcinogenic potency of asbestos and other fibrous dusts. *Staub-Rein. Luft* 38:486.

Pott, F., U. Ziem, F. J. Reiffer, F. Huth, H. Ernst, and U. Mohr (1987). Carcinogenicity studies of fibers, metal compounds, and some other dusts in rats. *Exp. Pathol.* 32:129–152.

Prenni, A. J., R. L. Siefert, T. B. Onasch, and M. A. Tolbert (2000). Design and characterization of a fluidized bed aerosol generator: A source for dry, submicrometer aerosol. *Aerosol Sci. Technol.* 32(5):465–481.

Prodi, V., T. De Zaiocomo, D. Hochrainer, and K. Spurny (1982). Fibre collection and measurement with the inertial spectrometer. *J. Aerosol Sci.* 13:49–58.

Rahjans, G. S., and J. L. Sullivan (1981). *Asbestos Sampling and Analysis.* Ann Arbor, MI, Ann Arbor Science.

Reid, A., G. Ambrosini, N. de Klerk, L. Fritschi and B. Musk (2004). Aerodigestive and gastrointestinal tract cancers and exposure to crocidolite (blue asbestos): Incidence and mortality among former crocidolite workers. *Int. J. Cancer* 111:757–761.

Ren, Z. F., Z. P. Huang, J. W. Xu, J. H. Wang, P. Bush, M. P. Siegal, and P. N. Provencio (1998). Synthesis of large arrays of well-aligned carbon nanotubes on glass. *Science* 282: 1105–1107.

Rickards, A. L. (1978). The routine monitoring of airborne asbestos in an occupational environment. *Ann. Occup. Hyg*. 21:315–322.

Rogak, S. N., U. Baltensperger, and R. C. Flagan (1990). Direct measurement of mass transfer to agglomerates in the transition regime. *J. Aerosol Sci.* 21(Suppl. 1):S51–S55.

Rogak, S. N., R. C. Flagan, and H. V. Nguyen (1993). The mobility and structure of aerosol agglomerates. *Aerosol Sci. Tech*. 18:25–47.

Rood, A. P., E. J. Walker, and D. Moore (1992). Construction of a portable fiber monitor measuring the differential light scattering from aligned fibres. *Aerosol Sci. Technol*. 17(1):1–8.

Rooker, S. J., N. P. Vaughan, and J. M. LeGuen (1982). On the visibility of fibres by phase contrast microscopy. *Am. Ind. Hyg. Assoc. J.* 43:505–515.

Rosner, D. E., D. W. Mackowski, and P. Garcia-Ybana (1991). Size- and structure-insensitivity of the thermophoretic transport of aggregated soot particles in gases. *Combust. Sci. Tech*. 80:87–101.

Sachweh, B., H. Barthel, R. Polke, H. Umhauer, and H. Buttner (1999). Particle shape and structure analysis from the spatial intensity pattern of scattered light using different measuring devices. *J. Aerosol Sci.* 30(10):157–1270.

Sampson, R. J., G. W. Mulholland, and J. W. Gentry (1987). Structural analysis of soot agglomerates. *Langmuir* 3:272–281.

Schmidt-Ott, A. (1988). In situ measurement of the fractal dimensionality of ultrafine aerosol particles. *Appl. Phys. Lett.* 52:954–956.

Schneider, J., S. Weimer, F. Drewnick, S. Borrmann, G. Helas, P. Gwaze, O. Schmid, M. O. Andreae, and U. Kirchner (2006). Mass spectrometric analysis and aerodynamic properties of various types of combustion-related aerosol particles. *Int. J. Mass Spectrom*. 258:37–49.

Schneider, T., E. Holst, and J. Skotte (1983). Size distribution of airborne fibres generated from man-made mineral fiber products. *Ann. Occup. Hyg*. 27(2):157–171.

Selikoff, I. J., and E. C. Hammond (1979). *Health Hazards of Asbestos Exposure*. New York, New York Academy of Sciences.

Shin, W. G., G. W. Mulholland, S. C. Kim, J. Wang, M. S. Emery, and D. Y. H. Pui (2009). Friction coefficient and mass of silver agglomerates in the transition regime. *J. Aerosol Sci.* 40:573–587.

Shin, W. G., G. W. Mulholland, and D. Y. H. Pui (2010). Determination of volume, scaling exponents, and particle alignment of nanoparticle agglomerates using tandem differential mobility analyzers. *J. Aerosol Sci.* 41:665–681.

Slowik, J. G., K. Stainken, P. Davidovits, L. R. Williams, J. T. Jayne, C. E. Kolb, D. R. Worsnop, Y. Rudich, P. F. DeCarlo, and J. L. Jimenez. (2004). Particle morphology and density characterization by combined mobility and aerodynamic diameter measurements. Part 2: Application to combustion-generated soot aerosols as a function of fuel equivalence ratio. *Aerosol Sci. Technol*. 38:1206–1222.

Smith, D. M., L. W. Ortiz, and R. F. Archuleta (1987). Long-term health effects in hamsters and rats exposed to man-made vitreous fibers. *Ann. Occup. Hyg*. 31(4B):731–754.

Sorensen, C. M. (1997). Scattering and absorption of light by particles and aggregates. In: *Handbook of Surface and Colloid Chemistry*, K. S. Birdi (ed.). Boca Raton, FL, CRC Press, pp. 533–558.

Sorensen, C. M. (2001). Light scattering from fractal aggregates. A review. *Aerosol Sci. Tech*. 35:648–687.

Sorensen, C. M. (2009). Scattering and absorption of light by particles and aggregates. *Handbook of Surface and Colloid Chemistry*, 3 ed., K. S. Birdi (ed.). Boca Raton, FL, CRC Press, pp. 719–745.

Sorensen, C. M., and G. D. Feke (1996). The morphology of macroscopic soot. *Aerosol Sci. Technol*. 25(3):328–337.

Sorensen, C. M., and G. C. Roberts (1997). The prefactor of fractal aggregates. *J. Coll. Inter. Sci.* 186:447–452.

Sorensen, C. M., and G. M. Wang (1999). Size distribution effect on the power law regime of the structure factor of fractal aggregates. *Phys. Rev. E* 60:7143–7148.

Sorensen, C. M., J. Cai, and N. Lu (1992a). Test of static structure factors for describing light scattering from fractal soot aggregates. *Langmuir* 8:2064–2069.

Sorensen, C. M., J. Cai, and N. Lu (1992b). Light-scattering measurements of monomer size, monomers per aggregate, and fractal dimension for soot aggregates in flames. *Appl. Optics* 31:6547–6557.

Sorensen, C. M., W. B. Hageman, T. J. Rush, H. Huang, and Oh. C. (1998). Aerogelation in a flame soot aerosol. *Phys. Rev. Lett.* 80:1782–1785.

Spurny, K. R., C. Boose, D. Hochrainer, and F. J. Mönig (1976). A note on the dispersing of fibrous powders. *Ann. occup. Hyg.* 19:85–87.

Spurny, K. R. (1980). Fiber generation and length classification. In: *Generation of Aerosols and Facilities for Exposure Experiments*,

K. Willeke (ed.). Ann Arbor, Ann Arbor Science Publishers. pp. 257–298.

Stanton, M. F., M. Layard, A. Tegeris, E. Miller, M. May, E. Morgan, and A. Smith (1981). Relation of particle dimension to carcinogenicity in amphibole asbestoses and other fibrous minerals. *J. Natl. Cancer. Inst.* 67:965–975.

Stayner, L., E. Kuempel, S. Gilbert, M. Hein, and J. Dement (2008). An epidemiological study of the role of chrysotile asbestos fibre dimensions in determining respiratory disease risk in exposed workers. *Occup. Environ. Med.* 65:613–619.

Stöber, W. (1971). A note on the aerodynamic diameter and the mobility of non-spherical aerosol particles. *J. Aerosol Sci.* 2(4):453–456.

Stöber, W. (1972). Dynamic shape factors of nonspherical aerosol particles. In: *Assessment of Airborne Particles*, T. T. Mercer, P. E. Morrow, and W. Stöber (eds.). Springfield, IL, Charles C. Thomas, pp. 249–289.

Stöber, W., H. Flachsbart, and D. Hochrainer (1970). Der aerodynamische durchmesser von latexaggregaten und asbestfasern. *Staub-Rein. Luft* 30:277–285.

Sussman, R. G., J. M. Gearhart, and M. Lippmann (1985). A variable feed rate mechanism for fluidized bed asbestos generators. *Am. Ind. Hyg. Assoc. J.* 46(1):24–27.

Tanaka, I., and T. Akiyama (1984). A new dust generator for inhalation toxicity studies. *Ann. Occup. Hyg*. 28(2):157–162.

Tanaka, I., and T. Akiyama (1987). Fibrous particles generator for inhalation toxicity studies. *Ann. Occup. Hyg*. 31:401–403.

Tanford, C. (1961). *Physical Chemistry of Macromolecules.* New York, John Wiley and Sons.

Timbrell, V. (1972). Alignment of carbon and other man-made fibers by magnetic fields. *J. Appl. Phys.* 43:4839–4840.

Timbrell, V. (1973). Desired characteristics of fibres for biological experiments. Fibres for biological experiments, Montreal, Canada, Institute of Occupational and Environmental Health.

Timbrell, V. (1975). Alignment of respirable asbestos fibres by magnetic fields. *Ann Occup. Hyg*. 18:299–311.

Timbrell, V. (1982). Deposition and retention of fibres in the human lung. *Ann. Occup. Hyg*. 26:347–369.

Timbrell, V. (1989). Review of the significance of fibre size in fibre-related lung disease: A centrifuge cell for preparing accurate microscope-evaluation specimens from slurries used in inoculation studies. *Ann. Occup. Hyg*. 33:483–505.

Timbrell, V., J. C. Gilson, and I. Webster (1968). Preparation of UICC reference asbestos materials. *Int. J. Cancer* 3:406.

Tolles, W. M., R. A. Sanders, and G. W. Fritz (1974). Dielectric response of anisotropic polarized particles observed with microwaves: A new method for characterizing the properties of nonspherical particles in suspension. *J. Appl. Phys.* 45(9): 3777–3783.

U.S. Environmental Protection Agency. (1985). Measuring airborne asbestos following an abatement action. EPA 600/4-85-049. EPA 600/4-85-049. Quality Assurance Division, Washington, DC. U.S. Environmental Protection Agency.

U.S. Environmental Protection Agency. (1987). Asbestos-containing materials in schools. Federal Register 40 CFR Part 763. Washington, DC, Government Printing Office. April 30, 1987, 40 CFR Part 763.

U.S. Environmental Protection Agency. (1989). Comparison of airborne asbestos levels determined by transmission electron microscopy (TEM) using direct and indirect transfer techniques. EPA 560/5-89-004. EPA 560/5-89-004. Washington, DC. U.S. Environmental Protection Agency.

U.S. Environmental Protection Agency. (1990). Managing asbestos in place: A building owners guide to operations and maintenance programs for asbestos containing materials. EPA 20T-2003. EPA 20T-2003. Washington, DC. U.S. Environmental Protection Agency.

U.S. Environmental Protection Agency. (2003). Final national primary drinking water rules: maximum contaminant level goals for inorganic contaminants. Washington, DC. U.S. Code of Federal Regulations Title 40 Part 141.51. EPA 816-F-03-016, June 2003. http://www.epa.gov/safewater/contaminants/index.html

Van de Hulst, H. C. (1957). *Light Scattering by Small Particles*. New York, John Wiley and Sons.

van de Vate, J. F., W. F. van Leeuwen, A. Plomp, and H. C. D. Smit. (1980). Dynamic shape factors: measurement techniques and results on aggregates of solid primaries. *J. Aerosol Sci.* 11:67–75.

Van Gulijk, C., J. C. M. Marijnissen, M. Makkee, J. A. Moulijn, and A. Schmidt-Ott. (2004). Measuring diesel soot with a scanning mobility particle sizer and an electrical low-pressure impactor: Performance assessment with a model for fractal-like agglomerates. *J. Aerosol Sci.* 35:633–655.

Virta, R. L., K. B. Shedd, A. G. Wylie and J. G. Snyder (1983). Size and shape characteristics of amphibole asbestos (amosite) and amphibole cleavage fragments (actinolite, cummingtonite) collected on occupational air monitoring filters. In: *Aerosols in the Mining and Industrial Work Environments*. V.A. Marple and B.Y.H. Liu (eds.). Vol. 2, pp. 633–643, Ann Arbor Science, Ann Arbor, MI.

Viscek, T. (1992). *Fractal Growth Phenomena.* San Francisco: World Scientific.

Walton, W. H. (1982). The nature, hazards, and assessment of occupational exposure to airborne asbestos dust: A review. *Ann. Occup. Hyg*. 25:115–247.

Wang, G. M., and C. M. Sorensen (1999). Diffusive mobility of fractal aggregates over the entire Knudsen number range. *Phys. Rev. E* 60:3036–3034.

Wegrzyn, J., and D. T. Shaw (1979). NUREG/CR-0799. Nuclear Regulatory Commission.

Weiss, M. A., A.-H. Cohen and I. Gallily (1978). On the stochastic nature of the motion of nonspherical aerosol particles. II. The overall drift angle in sedimentation. *J. Aerosol Sci.* 9:527–541.

Wen, H. Y., G. P. Reischl, and G. Kasper (1984). Bipolar diffusion charging of fibrous aerosol particles—I. Charging theory. *J. Aerosol Sci.* 15(2):89–101.

Weyel, D. A., M. Ellakkani, Y. Alarie, and M. Karol (1984). An aerosol generator for the resuspension of cotton dust. *Toxic. Appl. Pharm*. 76:544–547.

Whisnant, R. A. (1975). Evaluation of image analysis equipment applied to asbestos fiber counting. 210-75-0080/5. Cincinnati, OH, National Institute for Occupational Safety and Health.

Wiltzius, P. (1987). Hydrodynamic behavior of fractal aggregates. *Phys. Rev. Lett.* 58:710–713.

Witten, T. A., Jr., and L. M. Sander (1981). Diffusion-limited aggregation, a kinetic critical phenomena. *Phys. Rev. Lett.* 47:1400–1403.

World Health Organisation. (1997). Determination of airborne fibre number concentrations: A recommended method by phase contrast optical microscopy (membrane filter method). WHO, Geneva, Switzerland. 61 pp. www.who.int/occupational_health/publications/en/oehairbornefibre.pdf

Wu, M. K., and S. K. Friedlander (1993). Note on the power law equation for fractal-like aerosol agglomerates. *J. Coll. Interface Sci.* 159:246–247.

Wu, Z. F., and I. Colbeck (1996). Studies of the dynamic shape factor of aerosol agglomerates. *Europhysics Lett.* 33:719–724.

Wylie, A. G. (1979). Fiber length and aspect ratio of some selected asbestos samples. In: *Health Hazards Of Asbestos Exposure*, I. G. Selikoff and E. C. Hammond (eds.). New York, Annals NY Acad. Sci. 330:605–610.

Ye, J., X. Shi, W. Jones, Y. Rojanasakul, N. Cheng, D. Schwegler-Berry, P. A. Baron, G. J. Deye, C. Li, et al. (1999). Critical role of glass fiber length in TNF-a production and transcription factor activation in macrophages. *Am. J. Physiol. Lung C*. 276 (March (3 Pat. 1)):L426–L434.

Yu, P. Y., C. C. Wang, and J. W. Gentry (1987). Experimental measurement of the rate of unipolar charging of actinolite fibers. *J. Aerosol Sci.* 18(1):73–85.

Zelenyuk, A., and D. Imre (2007). On the effect of particle alignment in the DMA. *Aerosol Sci. Technol*. 41:112–124.

Zelenyuk, A., Y. Cai, and D. Imre (2006). From agglomerates of spheres to irregularly shaped particles: determination of dynamic shape factors from measurements of mobility and vacuum aerodynamic diameters. *Aerosol Sci. Technol*. 40:197–217.

Zhang, H. X., C. M. Sorensen, E. R. Ramer, B. J. Olivier, and J. F. Merklin (1988). In situ optical structure factor measurements of an aggregating soot aerosol. *Langmuir* 4:867–871.

Zimm, B. H. (1948). Apparatus and methods for measurement and interpretation of the angular variation of light-scattering, preliminary results on polystyrene solutions. *J. Chem. Phys.* 16:1099–1116.

Zumwalde, R. D., and J. M. Dement (1977). Review and evaluation of analytical methods for environmental studies of fibrous particulate exposures. DHEW (NIOSH) Publication No. 77-204. Cincinnati, OH, National Institute for Occupational Safety and Health.

EDQ1